NASA CR-54259
MTI-65TR2

GPO PRICE $

OTS PRICE(S) $

Hard copy (HC) 3.00

Microfiche (MF) 75

SECOND QUARTERLY REPORT

LUBRICATION ANALYSIS IN TURBULENT REGIME

by

F.K. Orcutt, C.W. Ng, J.H. Vohr, and E.B. Arwas

prepared for

NATIONAL AERONAUTICS AND SPACE ADMINISTRATION

CONTRACT NASw-1021

FACILITY FORM 602

N65 16201	
(ACCESSION NUMBER)	(THRU)
82	1
(PAGES)	(CODE)
CR54259	15
(NASA CR OR TMX OR AD NUMBER)	(CATEGORY)

MTI
MECHANICAL TECHNOLOGY INCORPORATED
research– development– manufacturing

NASA CR-54259
MTI-65TR2

SECOND QUARTERLY REPORT

LUBRICATION ANALYSIS IN TURBULENT REGIME

by

F. K. Orcutt, C. W. Ng, J. H. Vohr and E. B. Arwas

prepared for

NATIONAL AERONAUTICS AND SPACE ADMINISTRATION

January 30, 1965

CONTRACT NASw-1021

Technical Management
NASA Lewis Research Center
Cleveland, Ohio
Space Electric Power Office
Joseph P. Joyce
Robert T. Wainwright

MECHANICAL TECHNOLOGY INCORPORATED
968 Albany-Shaker Road
Latham, New York

TABLE OF CONTENTS

Page

SUMMARY 1

I. INTRODUCTION 2

II. THE DYNAMIC LOAD BEARING APPARATUS 4

III. THE TILTING-PAD JOURNAL BEARING 6
  A. Theoretical Analysis of the Tilting-Pad Bearing 7
  B. Experimental Study of the Tilting-Pad Bearing 8
    1. Static load capacity 9
    2. Frictional torque 11
    3. Dynamic load performance 12
    4. Critical speed analysis 13
    5. Response to dynamic load 14
    6. Hydrodynamic stability 16

IV. THE FLOATING-RING BEARING 17
  A. Floating-Ring Test Bearing Design 18
  B. Theoretical Analysis of the Floating-Ring Bearing 19

V. FUNDAMENTAL STUDY OF SUPERLAMINAR FLOW IN CONCENTRIC AND ECCENTRIC ANNULI 22
  A. Flow Visualization Using Electrochemiluminescence 22
  B. Torque and Pressure Measurements with Close Clearance Cylinders 23
  C. Studies Using Partial-Arc Bearings 25

REFERENCES 26

NOMENCLATURES: TILTING-PAD BEARING 27
FLOATING-RING BEARING 28

APPENDIX - ANALYSIS OF THE FLOATING-RING JOURNAL BEARING IN LAMINAR AND TURBULENT REGIMES A-1

FIGURES

SUMMARY

A major objective of this program is to develop and verify methods for design analysis of the most useful journal bearing configurations for high-speed rotary machinery using low kinematic-viscosity lubricants such as liquid metals.

The preloaded tilting-pad bearing has been tested experimentally. Measurements of static load capacity and shaft response to dynamic loading agree very well with calculated values and it is clear that, in these respects, the theoretical results are very adequate for design analysis. Measured torques are uniformly higher than the calculated values. The differences are probably due to losses in the test bearing seals, and separate experimental measurement of these losses is planned.

The analysis for static load properties of the floating-ring bearing has been completed and some numerical results are presented. The dynamic load analysis for this bearing is now being performed.

The second major objective is to prepare for future improvement of the basic superlaminar-flow lubrication theory by performing some studies of the fundamental processes of superlaminar flow in concentric and eccentric annuli. The apparatus is being prepared for experimental measurements of torque and film pressure between close-clearance concentric and eccentric cylinders with superlaminar flows. The experiments should begin early in February. The detailed design of the apparatus modification for partial-arc bearing experiments has been completed and fabrication of components has begun. Some preliminary experiments have been performed to evaluate the feasibility of using an electrochemiluminescence technique for flow visualization studies in very thin films, similar to those in bearings. Conclusive results have not yet been obtained, and further studies are planned.

I. INTRODUCTION

The objective of this program is to develop the means for rational design analysis of journal bearings for high-speed rotating machinery using lubricants of low kinematic viscosity. Under these circumstances, flow in the lubricant film of the bearings may become superlaminar. Water and liquid metals are examples of lubricants which will experience superlaminar flow with shaft speeds and bearing clearances which are characteristic of current practice in high-performance rotary machinery.

The program for development of a verified bearing design analysis for superlaminar-flow conditions can be broken into the following steps:

1. Formulate a practically useful turbulent-flow lubrication theory and develop the analysis for numerical calculation of static and dynamic load properties of the basic bearing elements (single partial arc and full cylinder).
2. Experimentally test the validity of the theory using single element bearings for a broad range of Reynolds numbers and other operating variables including both static and dynamic loading.
3. Using the verified theory, develop analyses of the most important, practical, composite-journal-bearing configurations and calculate their performance for a broad range of design variables and operating conditions including Reynolds number.
4. Verify the static and dynamic calculated performance characteristics of the composite bearings by experiment.
5. Throughout the program carry on a continuing study of the fundamental mechanics of superlaminar flow in bearings with the objective of improving the basic superlaminar flow lubrication theory.

The first two steps had been successfully completed by the end of the first part of this program (Refs. 1 and 2) and worthwhile progress had been made in the last area (Ref. 3). During the current contract, the third and fourth steps are to be completed and further progress will be made on the last. The journal bearing configurations which have been chosen for theoretical and experimental analysis are the tilting-pad and the floating-ring bearings.

During the first quarter, the turbulent-flow analysis of the tilting-pad journal bearing was completed and design analysis charts were prepared. Modifications to the dynamic-load bearing apparatus to accept the tilting-pad bearing and to measure bearing friction were completed. During this quarter, experimental testing of the tilting-pad bearing in the preloaded condition (m = 0.5) was completed. The static load analysis of the floating-ring bearing has been completed and some design curves are presented. In the study of flow fundamentals, preliminary experiments were performed using electrochemiluminescence as a flow visualization technique for close-clearance cylinders. Preparations are nearly complete for experimental studies of flow in a partial-arc configuration and for film pressure measurements between close-clearance cylinders.

II. THE DYNAMIC LOAD BEARING APPARATUS

The details of the construction and instrumentation of this apparatus were given in References 2 and 4. The arrangement of the test and support bearings on the shaft and the location and means of load application are illustrated schematically in Fig. 1. The test bearing diameter is four inches and the span between test and support bearings is 40 inches.

Shaft displacement is measured at both ends of the test bearing and at the support bearing by eddy-current sensors. Four of the same type of probes are mounted in the retainer ring so that they measure the proximity of the back surface of one of the pads at both ends of the roll and pitch axis (axial and circumferential oscillation respectively). These probes are connected as push-pull pairs to measure roll and pitch motions of the pad. The instrumented pad can be put in any position with respect to the unidirectional load but for all of the tests described here, it was on the loaded side of the bearing ahead of the unidirectional load line. The eddy-current gages are completely insensitive to whether air or silicone oil fills the gap between probe face and reference surface. They are sensitive to temperature changes and will experience zero drift for small changes and noticeable variation in sensitivity for large changes. To avoid this, the probes were located outside the test bearing housing in an ambient environment or they were connected in push-pull. During experiments, frequent checks for drift are made by stopping the shaft or operating with zero load to get a reference measurement — bottom of the clearance circle and bearing center respectively.

The shaft locus within the test bearing is displayed on one oscilloscope with d-c coupling by feeding the horizontal and vertical outputs into the x and y scope axes. In addition, any pair of dynamic components of shaft motion or pad motion can be switched into the inputs of a second dual trace oscilloscope where they can be displayed on the x-y axes or as two signals on a common time base. Variable electronic filters set for band pass operation are placed ahead of the inputs to this oscilloscope to eliminate unwanted high-frequency noise or subharmonic signals caused by fractional frequency whirl.

Unidirectional load is measured by a strain gage load cell to which the cable which applies the load is attached. Rotating load magnitude is determined by using unbalance slugs of a known weight at a known radius. Phase angle, between rotating load and shaft displacement, is measured by mounting a magnetic pickup on the vertical centerline so that it marks, with a voltage pulse, the instant when the unbalance slug is vertically up. This pulse is amplified and is then fed into the Z axis of the oscilloscope. This causes the intensity of the beam, or beams, to be reduced during the duration of the pulse, thus marking the instant when the unbalance force is directed upward by a break or interruption in the circular shaft locus orbit, or as cyclic breaks along the traces if the scope is set on time base. The angle between the spot of the beam interruption and the position where the shaft displacement is vertically up (the positive Y axis for X-Y presentation) is the phase angle.

Test bearing temperature is measured by a thermocouple welded onto the trailing edge of one of the loaded pads within 0.03 inch of the bearing surface. This is the temperature used for control purposes and to establish oil-film viscosity.

Frictional torque is measured by a Lebow strain-gage type, rotary torque sensor coupled into the drive between motor and support bearing end of the shaft. Full scale rating of the sensor is 200 inch-pound and it is linear within 0.1 percent.

The parasitic torque losses of the apparatus, including support and loader bearings and windage, were determined experimentally. An externally-pressurized, gas-lubricated journal bearing was designed, constructed and installed in place of the test bearing. The measured torques for a range of speeds and loads minus the calculated torque of the gas-lubricated bearing (using Petroff's equation) is taken as the parasitic torque characteristic of the machine. The results are given in Fig. 2. The torques are quite small and the effects of load are not uniformly consistent. Therefore, an average correction, independent of load, is made for each speed. The parasitic torque is subtracted from the total measured torque during experiments to give the test bearing torque. Further corrections for lubricant drag effects at the seals and for that portion of the shaft which is inside the test bearing housing but is not enveloped by the bearing have since been shown to be necessary. Plans for making this correction will be discussed later.

III. THE TILTING-PAD JOURNAL BEARING

The tilting-pad journal bearing consists of a set of partial-arc pads distributed around the shaft and individually pivoted as shown schematically in Fig. 3. The geometrical parameters that make up the design characteristics of the individual bearing are:

a. Bearing diameter (D)
b. Number of pads
c. Angular extent of the pads (β)
d. Slenderness ratio (L/D)
e. Pad clearance ratio (C_p/R)
f. Pivot location ($\frac{\theta_p}{\beta}$)
g. Pad mass and inertia
h. Geometrical preload coefficient (m)

Parameters f, g and h are peculiar to the tilting-pad bearing. Their significance is explained in some detail in Reference 4, and so they will be only briefly discussed here.

The pivot point location is crucial since it governs the inclination the pad will assume for a given shaft position, and hence the magnitude of the film hydrodynamic pressures.

Proper functioning of the tilting-pad bearing under dynamic load requires that the pads be able to track or follow the motion of the journal center. If the pads fail to track, the tilting-pad bearing will behave in a manner similar to that of the fixed pad bearing and may become subject to hydrodynamic film instability (fractional-frequency whirl). The ability of the pads to follow journal motions can be analyzed in terms of the inertia of the pad and the stiffness and damping of its fluid film. This has been done and the pad inertia (referred to as critical mass, M_{crit}) which must not be exceeded to ensure tracking has been calculated for the 80-degree arc, four-pad bearing (Ref. 4).

Geometrical preloading is used to achieve:

a. High bearing stiffness, even with zero net load on the shaft.
b. Positive fluid film pressures acting on all pads including those on the side away from the load direction.

Geometrical preloading is achieved by moving the pivot locations radially inward so that the clearance between the shaft, when centered in the bearing, and each pad at its pivot point is less than the machined clearance of the pads. Fig. 4 illustrates a tilting-pad bearing with and without preload. The preload coefficient is defined as:

$$\left(1 - \frac{\text{clearance at pivot location}}{\text{machined clearance}}\right)$$

The bearing used in the experimental studies, and therefore, the bearing which has been analyzed theoretically, has the following design characteristics:

Pad arc length (β) = 80 degrees (four pads)
Pivot position = .55 of the angular extent measured from the inlet edge.
Geometrical preload - Variable
Slenderness ratio (L/D) = 1.0
Clearance ratio (C_p/R) = $3.0\text{x}10^{-3}$ inch/inch
Pivot type - Ball (.625 radius) in internal cylindrical surface
(.655 inch radius)

The bearing pads are of hardened steel with about 10 mils of phosporous bronze spray coating on the bearing surface. The pivots are hardened-steel spherical-segment ends on short threaded rods which fit into an outer ring. The ball ends fit into a cylindrical groove cut into the back face of the pad so that the groove axis is parallel to the shaft axis. Preload is adjusted by turning the ball-end rods in or out. The adjustment is maintained by tightening set screws against the rods.

A. Theoretical Analysis of the Tilting-Pad Bearing

The theoretical analysis of the tilting-pad bearing including static and dynamic load properties is described in detail in Ref. 4. The calculations are based on the turbulent flow lubrication theory of Ng and Pan (Ref. 1). Calculated results for the four-pad, 80-degree arc, L/D = 1.0 bearing are presented in dimensionless form for values of preload coefficient of 0, 0.3, 0.5, and 0.7 and for Reynolds Numbers up to 16,000. The calculated results, and the experimental data, are all for the case of a static load direction midway between the pivots of the loaded pads. This is the bearing orientation which is normally used in practice. This arrangement also results in several helpful simplifications in the analysis. For example, the displacement of the shaft center caused by a change in load will be co-linear with the load, so the attitude angle is always zero. This, in turn, results in the elimination of the cross-coupling terms in the dynamic analysis reducing the number of dynamic coefficients from eight to four. A further simplification results from the fact that there are four pads. Since the resultant of the hydrodynamic force on each pad must pass through the pivots and since the pivots are located at 45 degrees from the load direction, the bearing reaction to a dynamic force superimposed on the static load will be equal for all directions of the dynamic force. This results in a further reduction in dynamic coefficients to two (one stiffness and one damping coefficient).

Calculated friction torque was omitted from Reference 4 because an error in the computer program affecting these results had been found. This has since been corrected and the results are given in Figs. 5 through 8.

B. Experimental Study of the Tilting-Pad Bearing

The static and dynamic load properties of the tilting-pad journal bearing will be measured for comparison with the calculated results for Reynolds Numbers up to 12,000 and for two values of preload coefficient, 0 and 0.5. The shaft speeds and oil viscosities used to obtain each value of Reynolds Number for both static and dynamic load experiments are given in Table 1. Two silicone oils are used in these experiments. One has a viscosity at 77 F of 5.0 cs and a viscosity-temperature coefficient $(1 - \frac{\text{viscosity at 210 F}}{\text{viscosity at 100 F}})$ of 0.55, and the viscosity of the other at 77 F is 0.65 cs with a coefficient of 0.31.

TABLE I

Reynolds Number $\frac{2\pi RNC_p \rho}{\mu}$	Shaft Speed rpm	Oil Viscosity centistokes
320 (Laminar)	2020	5.0
1000	4800	3.9 (100 F)
3000	2400	0.65
5000	4000	0.65
8000	6400	0.65
12000	8250	0.56 (110 F)

For each Reynolds Number, the Sommerfeld Number $\frac{\mu NLD}{W} (\frac{R}{C_p})^2$ was varied by changing the static load applied to the shaft. In all cases, the static load direction was midway between the pivots of the loaded pads.

Thus far, complete experimental data have been obtained for the case of $m = 0.5$ and results for $m = 0$ are now being obtained.

1. Static load capacity

The static load-carrying capacity results are given in Figs. 9 and 10, along with the corresponding theoretical results. The agreement is very good for all cases which continues the record of good correlation between theoretical and calculated load capacities obtained previously for the single partial-arc pad bearing over a similar range of operating conditions (Refs. 2 and 5).

The notation which is used for eccentricity ratio, $\epsilon_B(1-m)$, reduces to the eccentricity of the shaft center divided by the machined clearance of the pads (C_p). Thus, a displacement of the shaft center which is equal to the clearance at the pivots represents an eccentricity ratio of 1.0 for $m = 0$ and 0.5 for $m = 0.5$. Since the load direction is between pivots, it is possible to have eccentricities greater than the pivot clearance without contact between shaft and pads.

The measured shaft attitude angle was always zero as it should have been.

2. Frictional torque

Measured friction torque results are superimposed on the calculated curves in Figs. 11 and 12. Torque measurements were taken during the static load experiments. Providing the apparatus was operated at speed for 10 to 15 minutes before taking measurements to permit the torquemeter temperature to stabilize, the results were reproducible within about five percent at low speeds and less at high speeds. Torque was about 10 to 15 percent higher during dynamic load experiments than it was for the corresponding static load experiment. This would be expected because of vibration damping losses in the bearing.

The measured torques are consistently higher than the calculated results with the absolute difference being nearly uniform for all points at each speed (constant Re). The calculated values represent only the losses within the bearing itself. On the other hand, the measured losses include the seals at both ends of the test bearing housing and those due to "windage" from the sections of the shaft inside the bearing housing, but not enveloped by the bearing, as well as those from the bearing. The disparity points out the fact that an allowance for seal and windage losses should be added to calculated bearing losses in the design analysis for liquid-lubricated rotary machines.

In order to properly evaluate the correctness of the calculated bearing torque, experimental measurements of the seal and windage losses alone will be made. This will be done by supporting the test-bearing end of the shaft on the ball bearing which is normally used to apply static load. The test bearing will be removed but the seals will remain in place and lubricant will be circulated through the test bearing housing. Windage losses in the four-inch length of the shaft normally occupied by the bearing will be calculated and subtracted from the total torque along with the support bearing losses to give the test bearing seal and windage losses at each speed. This will be done upon completion of the tilting-pad bearing experiments and before proceeding to the floating-ring bearing.

The initial reduction of the experimental data for the high speed cases (6400 and 8250 rpm, giving Re = 8000 and 12,000 respectively) resulted in experimental load capacities which were considerably greater (lower eccentricity ratio) than were calculated. Further examination indicated that the centrifugal growth of the shaft at these speeds significantly affects the clearance. The increase in shaft radius was calculated to be 0.00071 inches at 8250 rpm and 0.000424 inches at 6400 rpm. A correction for this change in clearance was then made in all places where clearance appears in the dimensionless parameters for eccentricity ratio, torque, stiffness, damping and Sommerfeld Number for these speeds. This brought the measured static load capacity results into good agreement with the theoretical results as is shown in Figs. 9 and 10. The centrifugal growth of the shaft at the lower speeds is too small to be significant, so no corrections were required. For example, at 4000 rpm it is about 0.00017 inches which is close to the measurement accuracy for pad and shaft radii. The centrifugal growth of a shaft is much greater if the shaft is hollow, as this one is, so a correction should be made for such shafts running at high speeds and for solid shafts if the speeds are extremely high.

Corrections were required also for elastic deflection of the pivots under the static load since the displacement probes are mounted on the bearing housing and not on the pads. The correction was established by loading the non-rotating shaft and recording the indicated displacement for each load. The measured displacements were consistent with the calculated Hertzian deformation of the pivots. The correction is not a linear function of load, but it averages about 0.00032 inches per 100-pound load.

With the preloaded bearing, the pads are loaded internally by hydrodynamic action, even when there is no external load. Thus, pivot deflection is caused by shaft rotation alone and this should reduce the preload. This effect does not show up as a noticeable deviation in the measured and calculated results. The reason is probably the way in which the preload is adjusted. The preload pivot adjustment is made by inserting shims equal to the desired clearance between the shaft and each pad in the area of the pivot. The threaded ball-end rod is turned in until there is substantial resistance to a further advance, the shims are removed, and the pivot rod is locked in place by a set screw. In this way, the preload adjustment is made with a sizeable load on the pivots which tends to compensate for deflection due to internal hydrodynamic loading when the shaft is running.

3. Dynamic load performance

In rotating machinery design analysis, the dynamic properties of bearings are used as inputs to a rotordynamics analysis which determines:

a. Critical speeds of the rotor bearing system
b. Response of the rotor to unbalance or other dynamic load
c. Hydrodynamic stability boundaries of the rotor-bearing system.

For the investigation of bearing dynamic properties, the most direct and practical approach is to use the theoretical test-bearing dynamic properties to calculate the critical speeds, unbalance response and stability characteristics of the experimental apparatus. These calculated results can then be compared with the measured performance to evaluate the practical usefulness of the theoretical bearing properties.

The rotordynamics analysis is based on the assumption that for small amplitudes of motion the bearing fluid film forces can be linearized and expressed by means of spring and damping coefficients (Ref. 6). The method used in the analysis is that of Myklestad-Prohl (Ref. 7) which is an extension of the Holzer method. The rotor is represented by a finite number of mass points connected by weightless elastic elements. Thus, the rotor is divided into a suitable number of sections (in this case, eight) with each section having a constant stiffness along its length and with the mass of the section divided into two parts which are concentrated at the end points of the sections.

The MTI program provides for including the effects of pedestal flexibility. The pedestal is represented by a mass and a mass moment of inertia and is supported on springs and dashpots for both translatory and rotational motion. In these calculations, this feature is used to include the effects of bearing pivot flexibility. The elastic stiffness of the pivots was calculated and found to be $3.5\text{x}10^5$ pounds per inch at 100-pounds load (stiffness varies as the 2/3 power of load). The measured stiffness, obtained by measuring shaft deflection when loaded without rotation, was $3.12\text{x}10^5$ pounds per inch and it remained nearly constant over the range of load. A pedestal stiffness of $3.5\text{x}10^5$ pounds per inch was used for all conditions in the rotor dynamic analysis and the pad mass and mass moment of inertia were inserted. The pedestal damping and the stiffness for rotational motion were made equal to zero.

In the critical speed analysis, no bearing or pedestal damping is considered. The effect of this is to give somewhat lower critical speeds than will be the case if there is significant damping, especially pedestal damping. Bearing and pedestal damping are included in the unbalance response program.

The critical speed program searches the speed range for the given rotor configuration and bearing and pedestal characteristics and gives the system natural frequencies and the mode shape at each critical speed.

The unbalance response program computes the rotor deflections and the phase angle between the unbalance force and the shaft center displacement for each rotor mass point at a given speed. In addition, the pedestal motion and the force transmitted to the pedestal and to the foundation are given for each bearing location. In this program, comparison between the calculated and measured dynamic load properties of the test bearing is made by comparing shaft motion at the test bearing location. Shaft motion at the support bearing location was also monitored during the experiments but a comparison at this location is not very meaningful since the test bearing properties have very little influence on motion at the support bearing end. Moreover, the motions at the support bearing are quite small due to the arrangement of the bearings and unbalance force along the shaft.

4. Critical speed analysis

The calculated critical speed map of the rotor bearing system is given in Fig. 13. The support bearing stiffness was taken as $1.3\text{x}10^6$ pounds per inch (Ref. 8) for all conditions. The free-free natural frequency (zero bearing stiffnesses) is about 18,000 cpm. This mode occurs at 47,400 rpm for $1.3\text{x}10^6$ pounds per inch support bearing stiffness and $1.0\text{x}10^4$ pounds per inch test bearing stiffness. The first critical is a translatory mode and, for test bearing stiffnesses up to at least $2\text{x}10^5$ pounds per inch it is a rigid body vibration. Beyond $2\text{x}10^5$ pounds per inch test bearing stiffness, the critical speed plot begins to bend (critical speed is no longer proportional to test bearing stiffness only) indicating that there is beginning to be some effect of the support bearing or of shaft flexure. The second critical speed is a conical mode which changes very little with test bearing stiffness in the range of interest. This is reasonable in view of the high support bearing stiffness and the fact that the support bearing is at the extreme end of the shaft while the test bearing is about 1/4 of the shaft length in from the end. For these reasons, the support bearing characteristics largely control the conical mode.

The range of calculated test bearing stiffnesses ($m = 0.5$) for the experimental operating conditions (range of static load) for each Reynolds Number are indicated also in Fig. 13. In all cases, except Re = 12,000 (8250 rpm), the rotor-bearing system should be operating below the first critical speed. At 8250 rpm, the system should be very close to the first critical according to the critical speed analysis.

5. Response to dynamic load

Calculated curves of the radius of the circular locus orbit of the shaft center at the test bearing location in response to an unbalance force are given in Figs. 14 and 15. Corresponding experimental data points are superimposed on the calculated curves. Static load, W, was the experimental variable in the parameter, S, for a given Reynolds Number. The combinations of speed and viscosity given in Table I were used to obtain the indicated Reynolds Numbers. Corrections to the clearance, C_p, to account for centrifugal growth of the shaft were made for Re = 8000 and 12,000. The unbalance weight which was used varied depending on the speed and the test bearing stiffness. An unbalance weight was chosen to give an orbit diameter of from 0.1 to 0.2 times the radial pivot clearance (C_B) with 50 pounds load (shaft weight) at each Reynolds Number. Since the fluid film force of the bearing is linearized in the analysis, orbit radius is directly proportional to unbalance weight for a given set of operating conditions. Thus, all the results are presented as the orbit radius in inches per ounce-inch unbalance.

The shaft center orbits measured at the test bearing were characteristically circular and very stable. This is illustrated by the oscilloscope photograph, Fig. 16b, of the filtered, a-c component of the shaft displacement signal. The shaft motion at the support bearing end is much smaller, about 1/5 the size of the orbit at the test bearing. Figure 16a is a photograph of the orbit at the test bearing without filters and with d-c coupling. The high-frequency "hash" in the unfiltered signal is caused by magnetic inhomogenities of the shaft. The clearance "square" is shown also in Fig. 16a. The pivots are oriented at

45 degrees from the grid lines and this results in the characteristic square-on-edge shape of the clearance space for a four-pad bearing. The pviot clearance, C_B is half of the side of the square.

The measured and calculated phase angles, the angle by which the shaft center displacement lags the unbalance force, are given in Figs. 17 and 18 for the m = 0.5 bearing.

Agreement between the measured and calculated response of the shaft to unbalance loading is very good; better than has been the case in other work of this type (Refs. 6 and 9). Recognizing that these results cover just one value of bearing preload, it is clear that the combined lubrication-rotordynamics theory gave results which were precise enough for practical design analysis. The agreement between measured and calculated phase angles is not as good as it was for vibration amplitude. This is neither surprising nor especially serious since the interpretation of phase angles in rotor-bearing systems is frequently uncertain and, by themselves, they have no particular significance in design analysis.

The critical speed analysis indicated that operation at 8250 rpm (Re = 12,000) would be above the first critical speed. For a simple, rigid body, supported on a spring, one would expect a much larger vibration amplitude at this frequency than there was at lower frequencies and, in addition, the phase angle should be much larger at this frequency since there is a 180-degree shift in phase angle when passing through the critical speed. Neither of these expectations is realized in either the rotor response calculations or the experimental measurements at 8250 rpm. The absence of a higher vibration amplitude can be explained by the large amount of damping in this system. There is no such readily available explanation for the behavior of the phase angle. However, it is generally true that the phase angles in rotor systems, with their complex arrangements of multiple springs and dashpots representing the rotor, bearings and pedestals, do not behave in the straightforward fashion of a simple spring-mass system. The difficulty in making a meaningful interpretation of the phase angles which we have here is, unfortunately, characteristic of rotordynamics analysis at this time. Still, it is encouraging that the rotor response calculations and experiments do agree.

6. Hydrodynamic stability

As long as the pads track the motions of the journal center, the tilting-pad bearing should be hydrodynamically stable. The mass moment of inertia (M_{cr}) of the pads which must not be exceeded for proper pad tracking can be calculated from the theoretical curves of pad critical mass versus Sommerfeld Number given in Reference 4. This has been done for the operating conditions of these experiments. The resulting values of M_{crit} range from 0.1 to 0.32 $\text{lb.sec}^2/\text{in.}$ The actual mass moment of inertia of the pads M_{pad} is $6.7\text{x}10^{-4}$ $\text{lb.sec}^2/\text{in.}$ which is far less than the critical value. Therefore, there should have been no problem with pad flutter or hydrodynamic instability with the $m = 0.5$ preloaded bearing. This will be the case for any reasonable pad design with $m = 0.5$.

As was predicted, there was no evidence of instability for any operating condition, including zero load, for the bearing with $m = 0.5$. In addition, the pad motions, as measured by the probes mounted in the ring and referencing against the back of the pad, remained close to being in phase with the shaft motions. This is illustrated by the oscilloscope traces of the pad pitch and roll motions shown in Fig. 16. The interruption in the traces is caused by the unbalance force position marker and it indicates that at that time the force is directed vertically upward. If there were zero phase angles between unbalance force and shaft motion and between shaft and pad motions, the marker should occur at the midplane of the sinusoidal signal (zero tilt). Actually the markers occur about 70 degrees past the midplane (the beam sweeps from left to right). The unbalance force-shaft motion phase angles for these operating conditions were about 40 degrees, so the phase angle between shaft and pad motions is about 30 degrees.

The amplitude of the roll motion (cyclic, axial misalignment) remained fairly constant for all values of load and speed. The pitch and roll motions were usually nearly in phase, as shown in Fig. 16, although there were some small variations in the directions of a lag in roll of up to about 30 degrees.

IV. THE FLOATING-RING BEARING

The floating-ring bearing has been used successfully in many high-speed applications, especially in turbochargers. The basic bearing configuration is simple — a free, floating ring around the shaft with an outer bearing outside the ring. The main advantages are:

1. Low friction torque since the shaft drag is caused by shear of the inner film only. With the ring rotating at an intermediate speed, shear rates in this film are lower than they would be for a plain journal bearing at the same shaft speed and clearance. The torque reduction may be as much as half that of a fixed bearing whose clearance is equal to the shaft-to-ring clearance.
2. High lubricant flow through the bearing for a given pumping power because of the double films. This is especially significant in turbomachinery where bearing temperatures must be kept low in spite of close proximity to high temperature areas.
3. Very large damping because of the double lubricant films. This appears to be the explanation for the apparently good dynamic performance of the bearing at very high speeds, in spite of the fact that it lacks the inherent stability of the tilting-pad bearing.

Its disadvantages include:

1. Limited static load capacity compared with most other bearing types.
2. Erratic behavior at high eccentric ratios, probably because the ring speed is very sensitive to eccentricity in this range.
3. On start-up there may be some tendency for just one lubricant film to form so that the ring either rotates at shaft speed or remains stationary.

Design and application of floating-ring bearings have been done almost entirely by empirical means. There is a laminar-flow floating-ring bearing theory developed by Shaw (Ref. 10), but its practical value is restricted because:

1. It is for the infinite-length bearing case.
2. The effects of pressurized lubricant supply are not considered; yet these

bearings are nearly always supplied with lubricant under pressure. Pressurized lubricant supply will reduce the extent of film rupture in the bearing which will have an important effect, especially on the dynamic properties.

3. The solution covers only very large Sommerfeld Numbers corresponding to low eccentricity ratio.

A. Floating-Ring Test Bearing Design

The floating-ring test bearing has been designed and fabrication will soon begin. The design is similar to that used by Shaw and Nussdorfer (Ref. 10) in their experiments with a laminar flow bearing. The floating bushing is of steel coated with phosporous bronze. Lubricant is supplied to a circumferential groove at the centerline of the outer bearing ring (Fig. 19). There is a matching groove in the outer surface of the bushing and also a similar groove in its inner surface. Eight radial holes evenly spaced around the bushing communicate between the outer and the inner grooves. With this arrangement, lubricant is supplied under even pressure all around the circumference to both lubricant films at the bearing centerline. It then flows axially outward to ambient pressure at the ends.

The following bearing design parameters have been chosen:

Shaft diameter (D_1) = 4 inches

$L/D_1 = 1.0$

Ratio of bushing diameters $(\frac{D_2}{D_1}) = 1.2$

Inner film clearance ratio $(\frac{C_1}{R_1}) = 1.5\text{x}10^{-3}$ in/in.

Ratio of film clearances $(\frac{C_2}{C_1}) = 0.7$ and 1.3

Shaw and Nussdorfer reported irregular rotation of the bushing when the ratio of film clearance in their experiments was greater than 1.0. Bushing speed was stable and reproducible for values of C_2/C_1 of less than one. For this reason, we plan to use two values of C_2/C_1; one on either side of 1.0.

The position of the bushing within the outer bearing will be measured by four eddy-current probes; one on the X axis and one on the Y axis at each end of the bushing (Fig. 19). Bushing speed will be measured by putting an irregularity on the bushing surface at one end where it passes under the probes, resulting in a voltage peak once each revolution. This signal will be fed to an amplifier through a capacitance coupling and then into a frequency meter.

B. Theoretical Analysis of the Floating-Ring Bearing

The bearing model which has been analyzed consists of two load-carrying lubricant films, one on either side of the floating sleeve. Each lubricant film is supplied with oil under pressure from a circumferential groove at the centerline so that each film is divided into two bearings, each of slenderness ratio 1/2 and each having supply pressure at one end and ambient pressure at the other.

The first step in the analysis is to generate the basic data on the individual full-journal bearing film. This is done by a finite difference program to which the linearized turbulent flow lubrication theory (Ref. 1) is adapted. This results in a body of information on Sommerfeld Number, dimensionless torque and dimensionless flow for a range of assigned Reynolds Numbers, eccentricity ratios and dimensionless feed pressures. The procedure for obtaining this information is described in more detail in the Appendix.

For the composite floating-ring bearing, it is required that the supply pressure, load and torque for the inside and outside films must be equal. To do this, it is necessary to satisfy four equalities which are given in the Appendix. The Appendix also includes a brief description of the computational procedure for satisfying these equalities to obtain the floating-ring bearing static load performance curves given in Figs. 20 through 41. The computation and data reduction procedure is quite lengthy, so numerical results have been obtained just for the range of parameters which will be covered by the experiments, and just for L/D = 1.0 and R_2/R_1 = 1.2. If the theory is verified by the experiments, more extensive design curves can be prepared.

Static load capacity curves are given in Figs. 20 through 29. Shaft eccentricity in the ring, ϵ_1, versus Sommerfeld Number for four values of Reynolds Number is given in Figs. 20 through 25. Each figure gives results for one value of the outer to the inner film clearance ratio (C_2/C_1) and one value of the dimensionless supply pressure parameter $(\frac{P_s L D_1}{W})$.

The eccentricity of the ring in the bearing, ϵ_2, can be determined from Figs. 26 through 29 once ϵ_1 is known. The curves which are given for $C_2/C_1 = 1.3$ apply to all values of Reynolds Number. For this ratio of clearances, the differences with Reynolds Numbers are so small that variations in the curves due to numerical inaccuracies are of the same order.

The dimensionless friction factor $(\frac{R_1}{C_1} f)$ versus Sommerfeld Number is given in Figs. 30 through 35. Again, each figure gives data for one combination of C_2/C_1 and $\frac{P_s L D_1}{W}$ and for four values of Reynolds Numbers.

The ratio of ring speed to shaft speed (N_2/N_1) is given in Figs. 36 through 41 with the same arrangement for presentation. These results are similar to those of Shaw and Nussdorfer in that as the Sommerfeld Number becomes smaller (larger eccentricity), the ring-shaft speed ratio begins to fall rapidly. This effect accompanies and is related to the fact that at low Sommerfeld Numbers the outer film eccentricity ratio (ϵ_2) is becoming large while the inner film eccentricity (ϵ_1) is still small (Figs. 26 through 29).

The load capacities of the two films can be brought into better balance and a stable ring speed ratio can be maintained at lower Sommerfeld Numbers if the ratio of clearances, C_2/C_1, is kept below 1.0. This can be seen from a comparison of the results on ring speed ratio and ratio of film eccentricities for the two values of C_2/C_1 used in the calculations. On the other hand, a larger value of C_2/C_1 is desirable from the standpoint of friction torque reduction. Experiments with two values of C_2/C_1, one greater than 1.0 and one less than 1.0, were planned for the purpose of investigating these effects.

Indications are that the behavior of the bearing may be erratic in the range where N_2/N_1 changes rapidly with S. Shaw and Nussdorfer reported this and other field experience with the bearing also shows relatively poor behavior under high loads. According to Kettleborough, the main problem is to ensure formation of both hydrodynamic films when starting from rest under load. Neither Shaw and Nussdorfer nor Kettleborough gave any information on the displacement of the shaft or bushing in the bearing during their experiments (Kettleborough attempted such measurements but gave no results). The instantaneous measurements of shaft and ring locus and of shaft and ring speeds which are to be obtained in this program should reveal much about the operation of the bearing, especially at low Sommerfeld Numbers.

Thus far, the results on lubricant flow rate have not yet been reduced. This will be done in the near future and the static load results for the floating-ring bearing will then be complete. The dynamic load analysis is also proceeding and results should be obtained during the next quarter.

V. FUNDAMENTAL STUDY OF SUPERLAMINAR FLOW IN CONCENTRIC AND ECCENTRIC ANNULI

A. Flow Visualization Using Electrochemiluminescence

The test rig built to explore the use of electrochemiluminescence for studying flow patterns in bearings is shown in Fig. 42. The rig is a beaker in which there is a 5/8 inch I.D. glass sleeve. A 1/2 inch platinum-plated shaft, rotated by a variable speed drive, extends into the glass sleeve from above. This platinum-plated shaft is overcoated with an insulating layer of epoxy except for a one-inch long section within the glass sleeve. The platinum shaft is electrically connected to the positive terminal of a low-voltage d-c power supply. A platinum cathode is contained in the beaker. The entire beaker is filled with an electrochemiluminescent solution consisting mainly of water as solvent with KCL as a supporting electrolyte and Luminol* as the chemiluminescent substance. When a potential difference on the order of two volts is maintained between the platinum-plated shaft and the platinum electrode, a blue glow occurs in the film immediately adjacent to the surface of the platinum shaft within the glass sleeve (the part of the shaft not coated with epoxy). The intensity of this blue glow depends on the local rate of mass transfer of fresh solution to the surface of the rotating shaft. The glow pattern should reveal the onset of a Taylor vortex flow pattern or the onset of turbulence since these flow patterns will result in local variations in liquid mass transport at the shaft surface.

Experiments with the above test rig have been plagued by difficulties with the platinum plating on the shaft. All plated coatings of platinum tested to date have contained some microscopic pin holes with the result that the electrolytic solution quickly attacked the shaft beneath the platinum coating. Although we managed to obtain satisfactory glow patterns with the corroded shafts, no recognizable Taylor vortex flow pattern or turbulent flow pattern has yet been revealed by the electrochemiluminescent glow. It is thought that this may be due to the extreme roughness of the corroded shafts, which resulted in a considerable disturbance of the flow in the clearance between the shaft and the surrounding glass tube. In any case, because of the difficulties met within the development of the electrochemiluminescent technique, we have decided to concentrate our efforts on the other two experimental studies in the program, namely, the Studies Using Partial Arc Bearings and the Torque and Pressure Measurements with Close Clearance Cylinders. Progress on these two studies is discussed in separate sections below.

---

* Eastman Kodak Company Trade Name

We will continue to explore the feasibility of the electrochemiluminescent flow visualization technique for studying bearing flow. We are presently making a shaft using platinum foil rather than platinum plating and are confident that this will solve the corrosion problems. This new shaft will be tested within a week and we should soon know whether or not the electrochemiluminescent technique warrants further development for use in bearing studies.

B. Torque and Pressure Measurements with Close Clearance Cylinders

In last year's experimental work on the onset of Taylor vortices in the flow between non-concentric cylinders (Ref. 3), the test rig used had a clearance ratio that was quite large by bearing standards ($C/R_1 = 0.099$). Inertia effects were probably important in the flow and, therefore, there was some question concerning direct quantitative application of last year's results to bearings. In order to resolve this question, we plan to repeat last year's measurements using a test rig with a much smaller radial clearance. This test rig is shown schematically in Fig. 43. The inner aluminum cylinder is the one used in last year's experiments. The drive system, the method of varying eccentricities of the cylinders, and the method of measuring torque are also the same as employed last year and are described in Reference 3. The new outer cylinder, replacing last year's glass cylinder, is of aluminum and contains 16 pressure taps arranged circumferentially around the cylinder. The radial clearance between inner and outer cylinder is 0.02 inch, which results in a clearance to radius ratio of 0.011. Although this clearance ratio is still large compared with those occurring in bearings, it is nearly an order of magnitude less than the clearance ratio previously used, and by comparing the data obtained at $C/R_1 = 0.099$ and $C/R_1 = 0.011$, it should be possible to extrapolate the results to apply to bearings.

In the close clearance experiments, the onset of Taylor vortices will be detected by means of torque measurements alone. As described in Reference 3, this is the most precise way in which to determine Taylor vortex instability. Friction factor data will be taken in the Taylor regime and in the turbulent regime at different eccentricities. For concentric cylinders with outer cylinder stationary and inner cylinder rotating, the dependence of friction factor on clearance ratio is well established. For the case where the cylinders are eccentric, the friction factor data known to us is that taken at MTI last year ($C/R_1 = 0.099$) and some data taken by Smith and Fuller (Ref. 11) at a clearance ratio of 0.00293. These two sets of data do not agree qualitatively. It is believed that this disagreement is due to effects of "film rupture" in the Smith and Fuller tests. The non-concentric friction factor data to be taken in the present close clearance experiments coupled with the corresponding data taken last year should establish how eccentric cylinder friction factors depend on clearance ratio for the case of no film rupture.

Pressure distribution measurements in the close clearance experiments will be made by a monometer bank system. There will be sixteen manometers. The pressures at taps 2 through 16 will be measured simultaneously with respect to the pressure at tap 1 as reference. The fluid in the bottom on the manometers will be water with a specific gravity of 1.0. The fluid in the pressure tap lines and in the top of the manometer will be silicone fluid having a specific gravity in the range 0.873 to 0.960. Thus, a differential pressure of one inch of water will result in a monometer reading of the order of 10 to 20 inches. This degree of sensitivity is necessary since with two centistoke silicone oil (the viscosity grade to be used in the vortex instability runs) the maximum expected circumferential pressure difference at the Taylor critical speed will be on the order of only two inches of water at an eccentricity ratio of 0.5.

The pressure measurements to be made with the close clearance test rig will be valuable in two respects. First, the data will contribute to knowledge of bearing operating characteristics in superlaminar flow regimes and, second, knowledge of pressure gradient is necessary to compare theoretical prediction of flow instability with experiment.

The close clearance test rig described above is now being constructed and should be ready in January.

C. Studies Using Partial-Arc Bearings

Following the experiments with the close clearance test rig, it is planned to conduct visual studies of flow instability in a partial-arc configuration. The situation with respect to flow instability appears to be quite different in partial-arc geometries than it is in full cylindrical geometries. In the latter case, previous experimental results indicate that the flow in the wide region between full cylinders can be theoretically unstable locally to onset of Taylor vortices at speeds substantially below that at which vortices will actually first appear in the flow. This indicates that the stability of the flow at any point depends not upon local conditions alone, but is influenced by the flow conditions all around the cylinders. On the other hand, early tests with a partial-arc bearing (Ref. 5) show evidence that vortices do form when the local flow in the entrance regions of these bearings becomes theoretically unstable. Whether this indeed does occur and whether it is due to the smaller C/R ratio of the partial-arc bearing (the above mentioned study of Taylor instability between full cylinders was for the case of much larger C/R) or is characteristic of partial-arc geometries in general are questions which we expect to answer by means of the planned partial-arc studies. The test rig for these studies is shown schematically in Fig. 44. It consists essentially of a 80 degree plexiglas partial-arc bearing mounted within an aluminum outer tube. The inner cylinder will be the same as that used in the close clearance rig. Radial clearance between the plexiglas "bearing" and the inner cylinder will be 1/8 inch. Five circumferential pressure taps will be located to measure the pressure along an arc of the "bearing". The plexiglas bearing will be able to be positioned to provide any arrangement of converging, diverging, converging-diverging or diverging-converging channel. Except for the pressure distribution measurements, which are necessary to compare theoretically predicted instability speeds with those measured experimentally, the study will be a visual one. Flow visualization will be by means of aluminum powder suspended in the silicone test fluid.

The detail design of the partial-arc test rig described above has been completed and construction of the rig will begin in January.

REFERENCES

1. Ng, C. W. and Pan, C. H. T., "A Linearized Turbulent Lubrication Theory" ASME Paper 64-Lub-29, presented at the International Lubrication Conference, Washington, D.C., October, 1964.

2. Orcutt, F. K., and Arwas, E. B., "Analysis of Turbulent Lubrication, Volume 1, The Static and Dynamic Properties of Journal Bearings in Laminar and Turbulent Regimes," MTI 64TR19, Final Report on NASA Contract NAS-W-771, May 1964.

3. Vohr, J. H., "Analysis of Turbulent Lubrication, Volume 2, An Experimental Study of Vortex Flow and Turbulence in Concentric and Eccentric Annuli," MTI 64TR20, Final Report to NASA on Contract NAS-W-771, May 1964.

4. Orcutt, F.K., Ng, C.W., Vohr, J. H. and Arwas, E.B., "Lubrication Analysis in Turbulent Regime," First Quarterly Report, NASA CR-54195, MTI 64TR57, October 1964.

5. Orcutt, F. K., "Investigation of a Partial Arc Pad Bearing in the Superlaminar Flow Regime", ASME Paper 64-LubS-8, presented at the Lubrication Symposium at Cleveland, Ohio, April 1964.

6. Lund, J. W., "Spring and Damping Coefficients for the Tilting Pad Journal Bearing," ASLE Paper 64AM-2B3, presented at the Annual Meeting, Chicago, May 1964.

7. Prohl, M. A., "A General Method for Calculating Critical Speed of Flexible Rotors," Trans. ASME, 1945, pp. A142-A148.

8. "Design Data for Ball Bearings," MTI 64TN11.

9. Warner, P. C. and Thoman, R. J., "The Effect of the 150 Degree Partial Bearing on Rotor Unbalance Vibration," ASME Paper 63-LubS-6.

   Also:

   Lund, J. W., Discussion to the above paper.

10. Shaw, M. C. and Nussdorfer, T. J., "An Analysis of the Full-Floating Journal Bearing," NACA Research Memorandum E 7A28a.

11. Smith, M. I., and Fuller, D. D., "Journal Bearing Operation of Superlaminar Speeds," ASME Paper 55 Lub-26, 1955.

NOMENCLATURE FOR TILTING-PAD BEARING

a - Geometrical Preload, inches

B - Damping Coefficient, lb.sec/inch

C_B - Bearing Radial Clearance ($= C_P(1-m)$), inches

C_P - Pad Radial Clearance (= Radius of curvature of Pad - Radius of curvature of shaft), inches

D - Diameter, inches

e_B - Bearing Eccentricity (= Distance between journal and bearing centers), inches

e_P - Pad Eccentricity (= Distance between center of journal and center of curvature of pad), inches

F - Force, lbs.

F_o - Steady State Force, lbs.

F_x, F_y - Components of Dynamic Force, lbs.

f - Coefficient of Friction

K - Stiffness Coefficient, lbs/inch

L - Length, inches

m - Geometrical Preload Coefficient ($= \frac{a}{C_P}$)

M_{crit} - Critical Mass of Bearing Pad, lbs.sec^2/inch

N - Speed, R.P.S.

Q - Flow into Bearing Pad, in^3/sec.

Q_s - Side Leakage Flow, in^3/sec.

R - Radius, inches

Re - Reynolds Number ($= \pi DNC_P\rho/\mu$)

S - Sommerfeld Number ($= \frac{\mu NLD}{W}(\frac{R}{C_P})^2$)

W - Bearing Load (= Vector sum of the loads on the individual pads), lbs.

x, y - Co-ordinates, inches

β - Angular Extent of Pad, degrees

ϵ_B - Bearing Eccentricity Ratio ($= \frac{e_B}{C_B}$)

ϵ_P - Pad Eccentricity Ratio ($= \frac{e_P}{C_P}$)

θ_P - Angular Distance of Pivot Point from inlet of Pad, degrees

ρ - Mass Density, $\frac{\text{lb.sec}^2}{\text{in}^4}$

ω - Angular Speed, radians/second

NOMENCLATURE FOR FLOATING-RING BEARING

C = Radial clearance

F = Frictional force

F_t = Tangential force

f = $\frac{F}{W}$

N = Revolution per second

P_s = Circumferential supply pressure

P_D = $P_s/\mu N \left(\frac{R}{C}\right)^2$

R = Radius

R_1 = Radius of shaft and inside radius of the floating sleeve

R_2 = Outside radius of the sleeve and inside radius of the bearing

Re_s = $2\pi R_1 C_1 N_1/\nu$ Shaft Reynolds Number

Re_1 = $2\pi R_1 C_1 (N_1 - N_2)/\nu$

Re_2 = $2\pi R_2 C_2 N_2/\nu$

S = Sommerfeld Number = $\mu NLD\left(\frac{R}{C}\right)^2/W$

T = Torque = RF

W = Unidirectional load

α = N_2/N_1

ϵ = Eccentricity ratio

ν = Kinematic viscosity

Subscript

1	Refer to the shaft
2	Refer to the floating sleeve
m	Refer to the mean values
s	Refer to the shaft operating condition

APPENDIX - ANALYSIS OF THE FLOATING-RING JOURNAL BEARING IN LAMINAR AND TURBULENT REGIMES

The bearing consists of two load-carrying oil films, one inside the floating sleeve, and the other outside. Shear of the inside film tends to make the floating sleeve rotate with the journal, whereas the shear in the outer oil film tends to retard the rotation. Therefore, an equilibrium velocity for the floating sleeve can be established.

Computation of Basic Full-Journal Bearing Data

It can be imagined that each oil film is an individual full journal bearing. Further, the model to be studied is pressure-fed from the centerline of the outside bearing and the floating sleeve has radial holes interconnecting the films such that each film can be divided into two parts, each with a slenderness ratio of 1/2. Now, the full-journal bearing is pressurized on one side, while the other side is at ambient pressure and the pressure distribution is no longer symmetric with respect to the centerline. A numerical finite difference program is written to compute the properties of this bearing for both laminar and turbulent flows. The linearized turbulent lubrication theory, established by Ng and Pan (Ref. 1) is adapted for the computer program.

If it is assumed that the inertia effect of the floating ring is negligible, the torques and the loads for the inner and outer films must be equal in order to achieve the equilibrium condition.

Since the clearance of the ring is much smaller than the radial dimension, it is reasonable to assume the inside radius of the bearing is the same as the outside radius of the sleeve and inside radius of the sleeve is the same as the shaft radius.

The dimensionless quantities given below are standard for the full journal bearing with circumferential feeding. The speed of the shaft and of the floating sleeve lead to the consideration of the Reynolds Number.

$$Re = \frac{VC}{\nu} = \frac{2\pi RNC}{\nu}$$

where N is speed in revolutions, C is the bearing clearance and ν is the kinematic viscosity.

The circumferential feeding pressure can be expressed in dimensionless form as

$$P_D = \frac{P_s}{\mu N(\frac{R}{C})^2}$$

The computed information on the full journal bearing includes the load, torque and the flow. These are represented as:

The Sommerfeld Number: $S = \mu NLD\ (R/C)^2/W$

The Dimensionless Tangential Force: $\bar{F}_t = \dfrac{F_t}{\mu NLD(R/C)^2}$

The Dimensionless Flow: $Q/RCNL$

The Dimensionless Torque: $Rf/C = RF/CW$

where F is the frictional force and f is the friction coefficient $(f = \frac{F}{W})$.

The eccentricity ratio, the Reynolds Number and the dimensionless circumferential feed pressure are the parameters in constructing a table for load and torque of the single full-journal bearing. The feeding pressure is conveniently correlated by introducing the load factor, P_sLD/W, which is equal to the product of P_D and S. Considering the operating conditions of the experimental set-up, such as the speed range of the shaft, the load limit and the geometrical dimension of the bearing, the range within which the P_DS or P_sLD/W (load factor) must lie is from zero to fifty.

P_D is an input parameter for the full-journal bearing program and S is an output variable. In order to select values of P_D which will keep the load factor P_DS within the range of 0 to 50, a trial run was made with a range of values for P_D with constant Re and ϵ in order to establish a proper range for P_D.

The full-journal bearing program is used to construct a table in which S, R/C f and F_t are given for each combination of P_D, Re and ϵ. Seven values of Re are used covering the range from 100 (laminar) to 10,000. The six eccentricity ratios used are: 0.01, 0.05, 0.1, 0.3, 0.5 and 0.7. Unsatisfactory correlation of the data on S and R/C f excluded higher eccentricity ratios. Since P_s is equal for both films, there will be different values of $\frac{P_s LD}{W}$ for the two films for the same operating conditions with the difference being proportional to R_2/R_1. Therefore, a second table is prepared for the outer film using values of $\frac{P_s LD_2}{W}$ which correspond to those of $\frac{P_s LD_1}{W}$ used in the inner film table.

Analysis of the Composite Floating-Ring Bearing

The floating-ring bearing analysis presented by Shaw (Ref. 10) utilizes the infinite closed solution for a full-journal bearing with no pressurized feeding under the laminar condition. Finite slenderness ratio, circumferential pressurized feeding and operation in the turbulent flow region add extra complications in comparison with Shaw's simplified analysis. Film rupture and the effect of feed pressure on film rupture are also taken into account in the present analysis.

To combine the inner and outer films for the floating-ring bearing, it is required that the supply pressure (P_s), load, and torque for both films must be equal. This implies that the two sets of full-journal bearing data for a given load factor, $P_s LD/W$, and radius ratio, R_2/R_1, must satisfy the following equalities where the subscript 1 refers to the shaft and inner film and 2 refers to the ring and outer film:

1) The ratio of Reynolds Numbers

$$\frac{Re_1}{Re_2} = \frac{R_1}{R_2} \frac{C_1}{C_2} \left(\frac{N_1}{N_2} - 1 \right) \qquad \text{(A-1)}$$

where $Re_1 = \frac{2\pi \, R_1 C_1 \, (N_1 - N_2)}{\nu}$, $Re_2 = \frac{2\pi \, R_2 C_2 N_2}{\nu}$

2) Equality of supply pressure for the two films requires:

$$\left.\frac{P_s LD}{W}\right._1 = \frac{R_1}{R_2} \left(\frac{P_s LD}{W} \right)_2 \qquad \text{(A-2)}$$

3) Equality of load carried by the two films requires:

$$\frac{S_1}{S_2} = \left(\frac{R_1}{R_2}\right)^3 \left(\frac{C_2}{C_1}\right)^2 \left(1 + \frac{N_1}{N_2}\right) \qquad \text{(A-3)}$$

with $W_1 = W_2$, where $S_1 = \mu(N_1+N_2)\, LD_1 \left(\frac{R_1}{R_2}\right)^2 \Big/ W_1$ and $S_2 = \mu N_2 LD_2 \left(\frac{R_1}{R_2}\right)^2 \Big/ W_2$.

4) Equality of inside and outside torques on the floating ring implies:

$$\left(\frac{R_1}{C_1} f_{m1} \frac{(1-\alpha)}{(1+\alpha)} - \frac{\epsilon_1}{2} S_1 \bar{F}_{t1}\right) \Bigg/ \left(\frac{R_2}{C_2} f_{m2} + \frac{\epsilon_2}{2} S_2 \bar{F}_{t2}\right) = C_2/C_1 \qquad \text{(A-4)}$$

with $T_1 = T_2$, where $\alpha = N_2/N_1$

The subscript m refers to the mean value.

The computational procedure is outlined below :

a) Assign load factor and R_2/R_1. Two tables, one for the inner film and one for the outer film, of S, Rf_m/C_1 and $\bar{F}_t$ are given for each combination of six eccentricity ratios and seven Reynolds Numbers. Equation (A-2) is implicitly satisfied.

b) Select a value of C_2/C_1, $Re_s = \dfrac{2\pi R_1 C_1 N_1}{\nu}$ and ϵ_1.

c) Set several values for N_2/N_1.

d) Calculate Re_1 using Eq. (A-1).

e) With known Re_1 and ϵ_1; S_1, Rf_{m1}/C and $\bar{F}_{t1}$ can be calculated through interpolation from Table 1.

f) Calculate Re_2 using Eq. (A-1) and S_2 from Eq. (A-3).

g) Use interpolation with known Re_2 and S_2 to find ϵ_2 from Table 2.

h) Use ϵ_2 to find Rf_{m2}/C and $\bar{F}_{t2}$ from Table 2.

i) Check Eq. (A-4) for equality; if not satisfied, a new value of N_2/N_1 is selected. The steps from (d) on are repeated.

j) A quadratic interpolation is used to determine the exact N_2/N_1 ratio within a specified error limit of one percent allowed for Eq. (A-4).

k) With N_2/N_1 known, the bearing Sommerfeld Number, $S = \frac{\mu N_1 D_1 L}{W}\left(\frac{R_1}{C_1}\right)^2$ and the dimensionless shaft torque $f\frac{R_1}{C_1} = F_{m1}\frac{R_1}{C_1} + \epsilon_1 S_1 \overline{F}_{t1}/2$ can be calculated for the conditions which have been assigned; namely, R_2/R_1, C_2/C_1, Re_s and $p_s LD_1/W$.

FIGURES

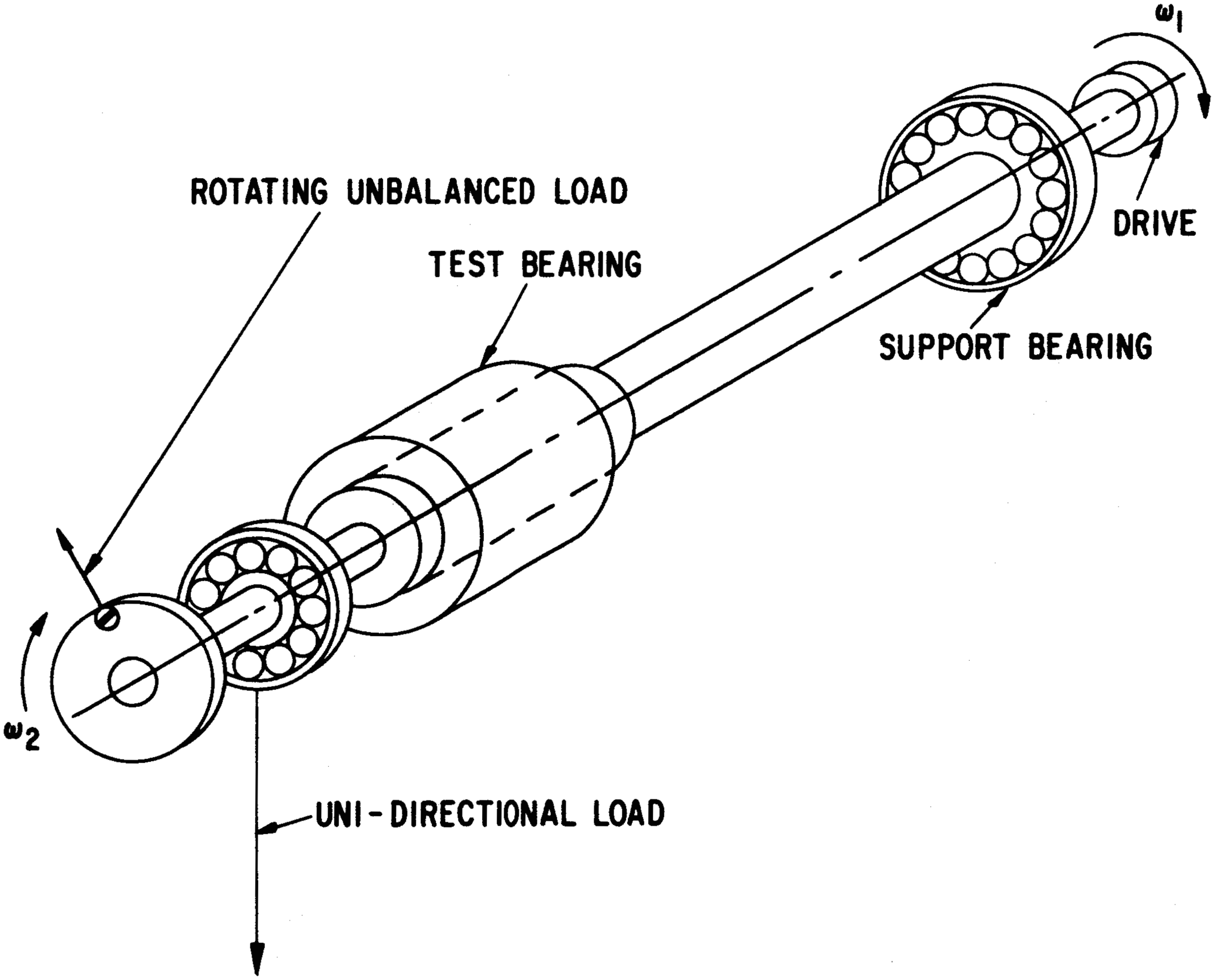
ω1
ROTATING UNBALANCED LOAD
TEST BEARING
DRIVE
SUPPORT BEARING
ω2
UNI-DIRECTIONAL LOAD

Fig. 1 Schematic of Apparatus Shaft and Bearing Assembly

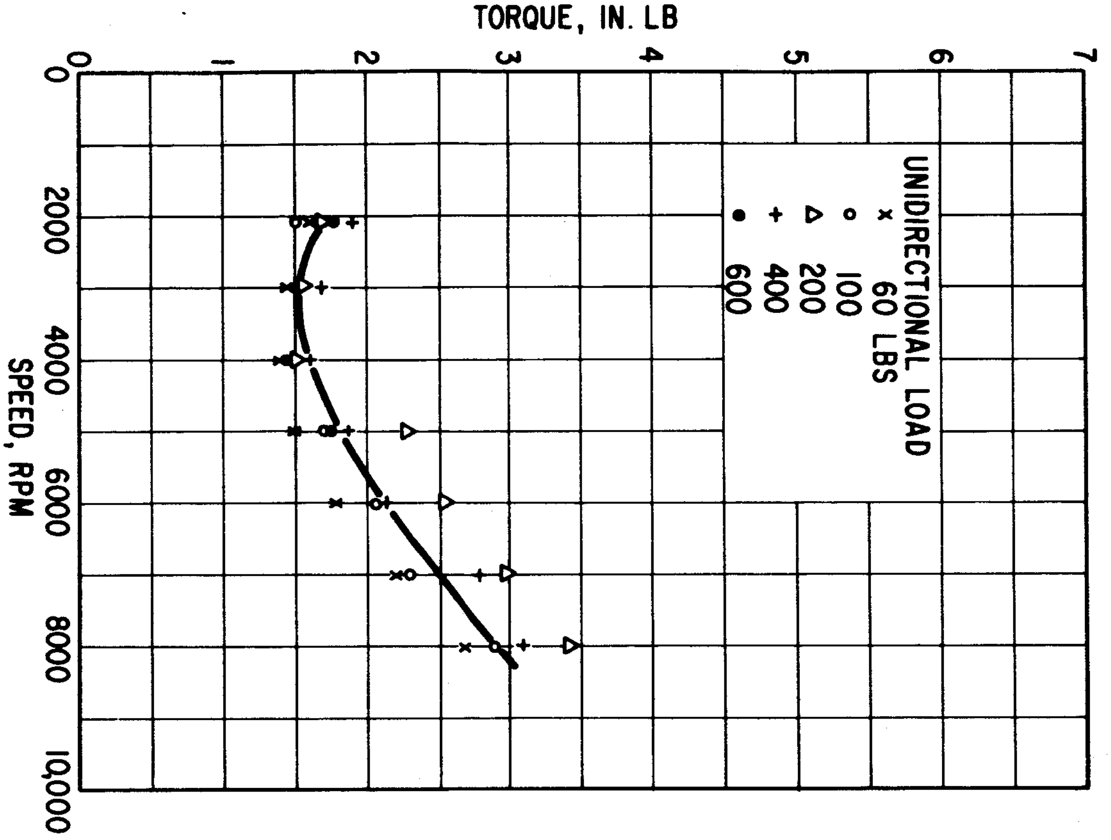

Fig. 2 Dynamic Load Bearing Apparatus Parasitic Torque Measurements

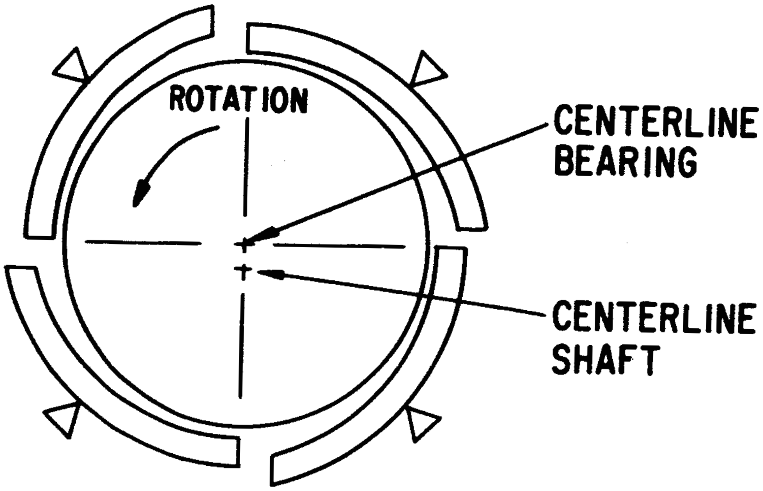
ROTATION
CENTERLINE BEARING
CENTERLINE SHAFT

Fig. 3 Schematic of Tilting Pad Bearing.

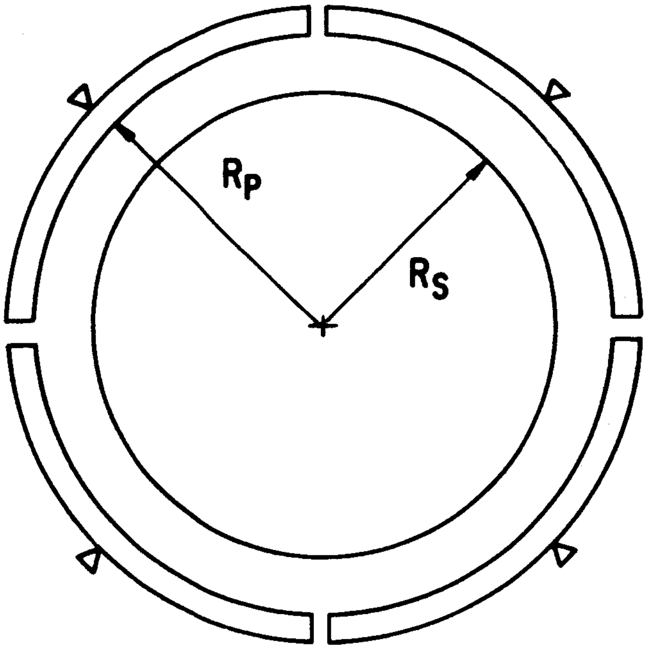

4 PAD BEARING
ZERO PRELOAD
(a)

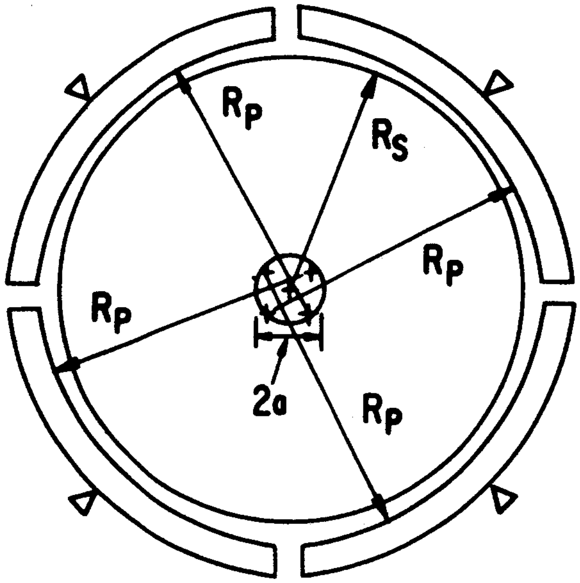
R_P
R_S
R_P
R_P
2a
R_P

4 PAD BEARING
PRELOAD = a
(PRELOAD COEFFICIENT = $\frac{a}{R_P - R_S}$)
(b)

Fig. 4 Geometrical Arrangement of Pads

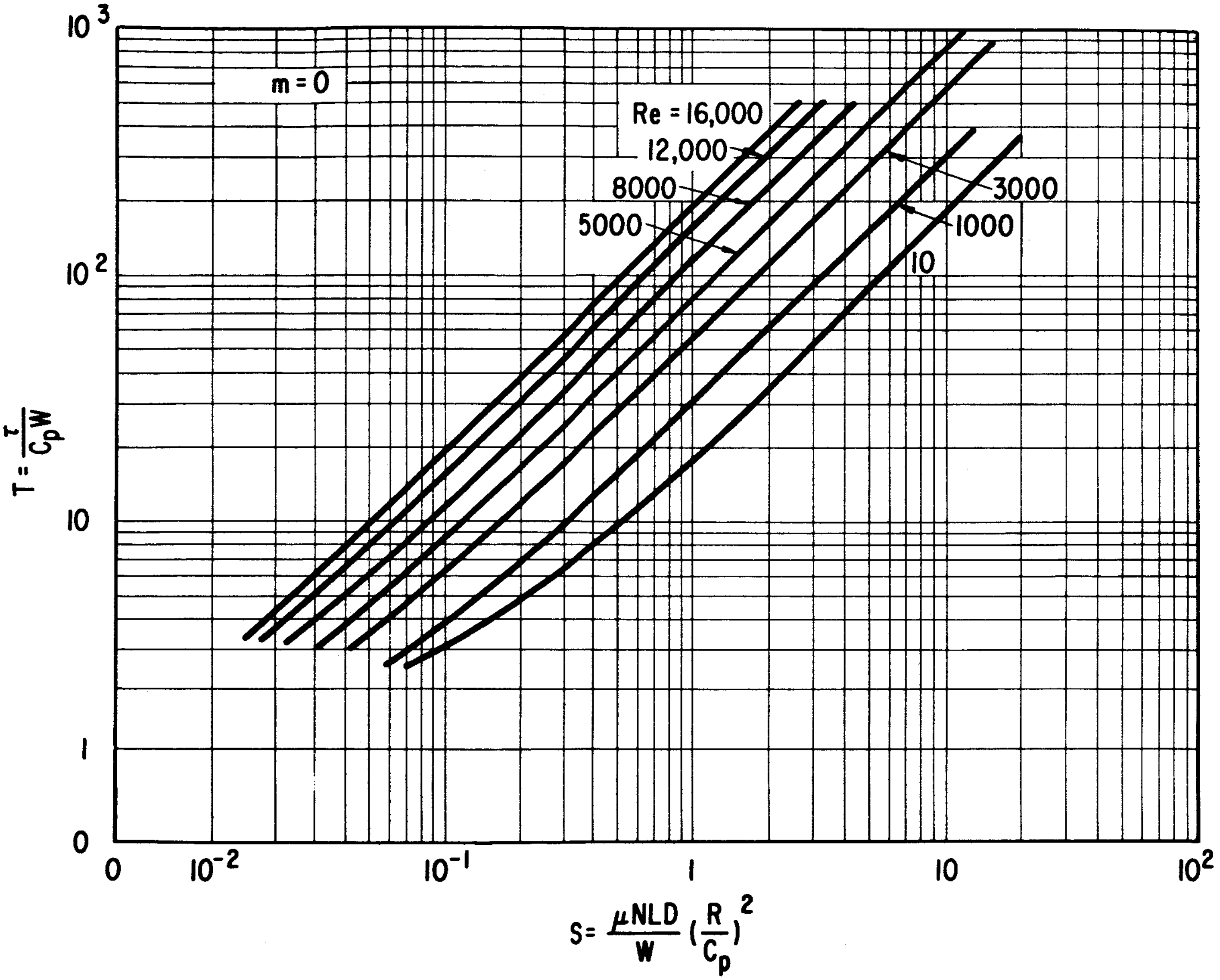

Fig. 5 Tilting-Pad Bearing Theoretical Friction Torque
$m = 0$, 4 pads, $\beta = 80^{o}$, $\theta_p = .55$, $L/D = 1.0$

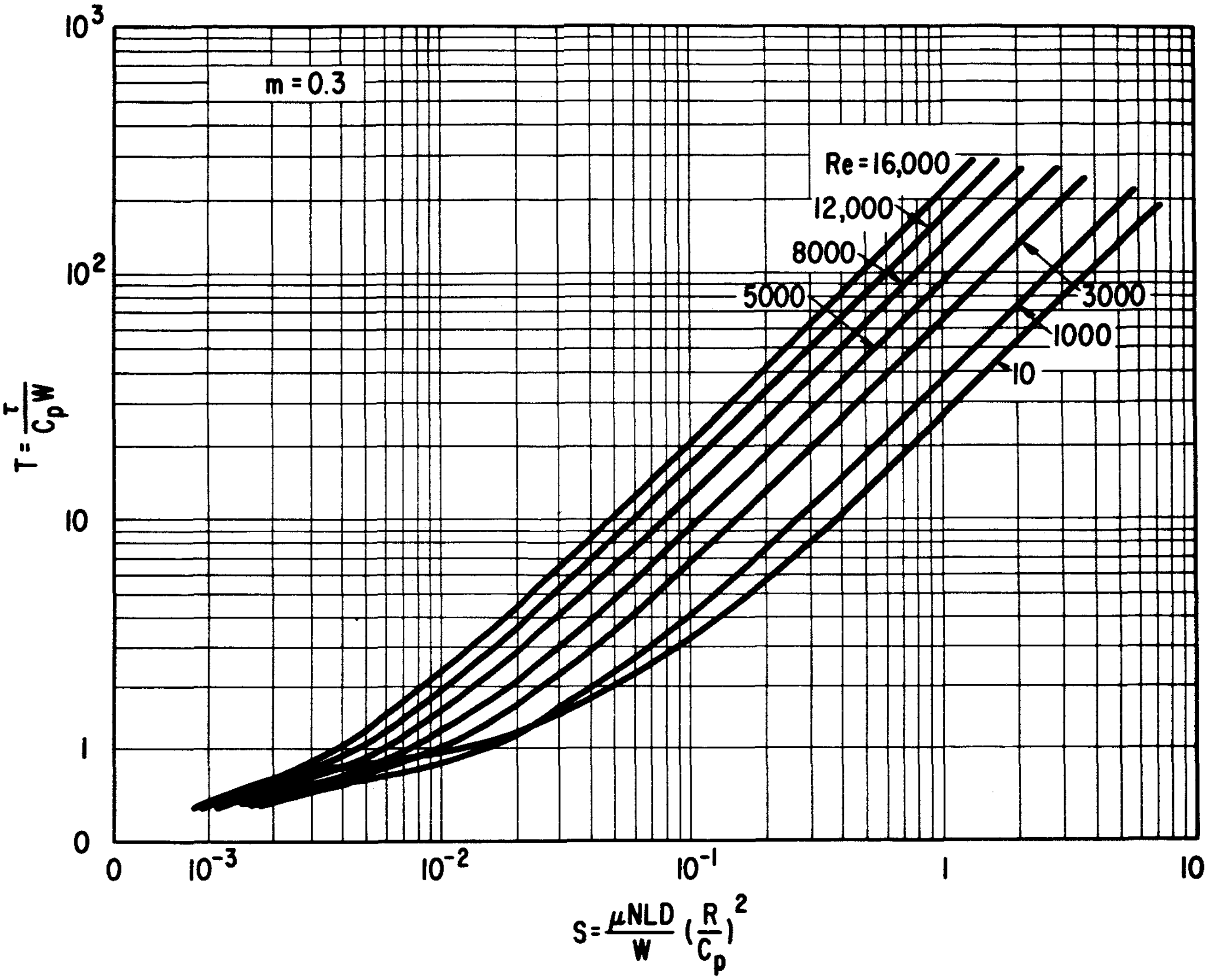

Fig. 6 Tilting-Pad Bearing Theoretical Friction Torque
$m = 0.3$, 4 pads, $\beta = 80^o$, $\theta_p = .55$, $L/D = 1.0$

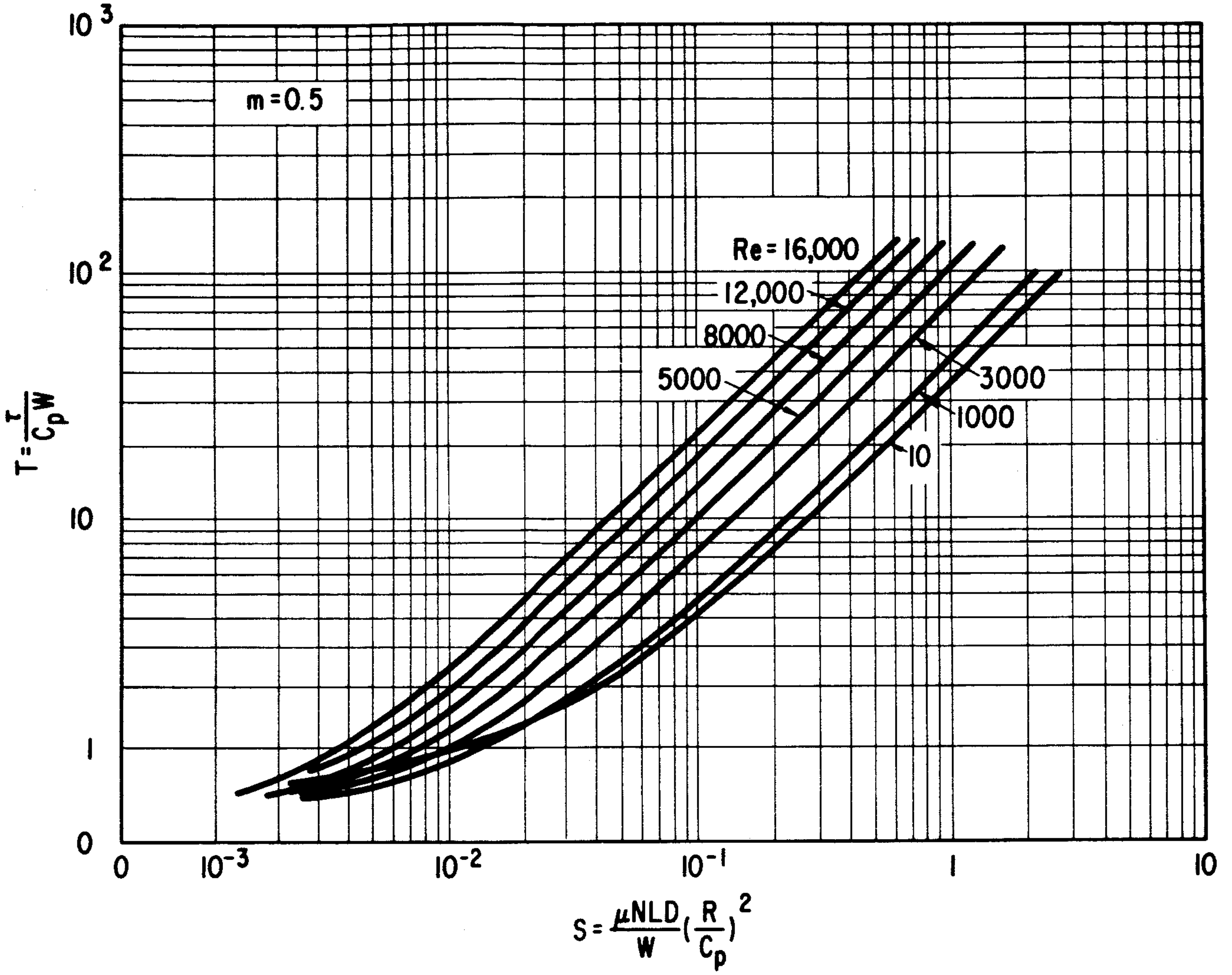

Fig. 7 Tilting-Pad Bearing Theoretical Friction Torque
$m = 0.5$, 4 pads, $\beta = 80^\circ$, $\theta_p = .55$, $L/D = 1.0$

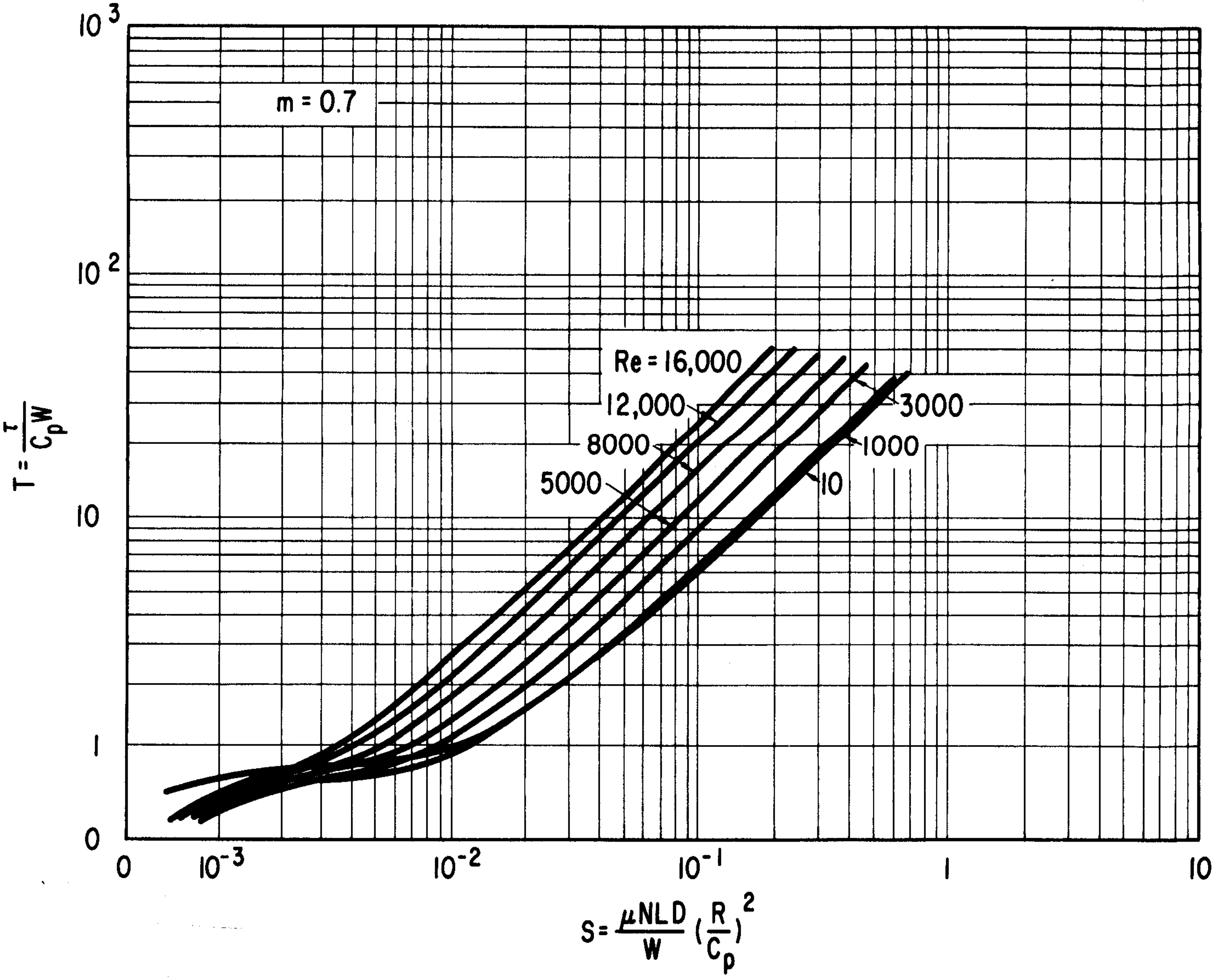

Fig. 8 Tilting-Pad Bearing Theoretical Friction Torque
$m = 0.7$, 4 pads, $\beta = 80^\circ$, $\theta_p = .55$, $L/D = 1.0$

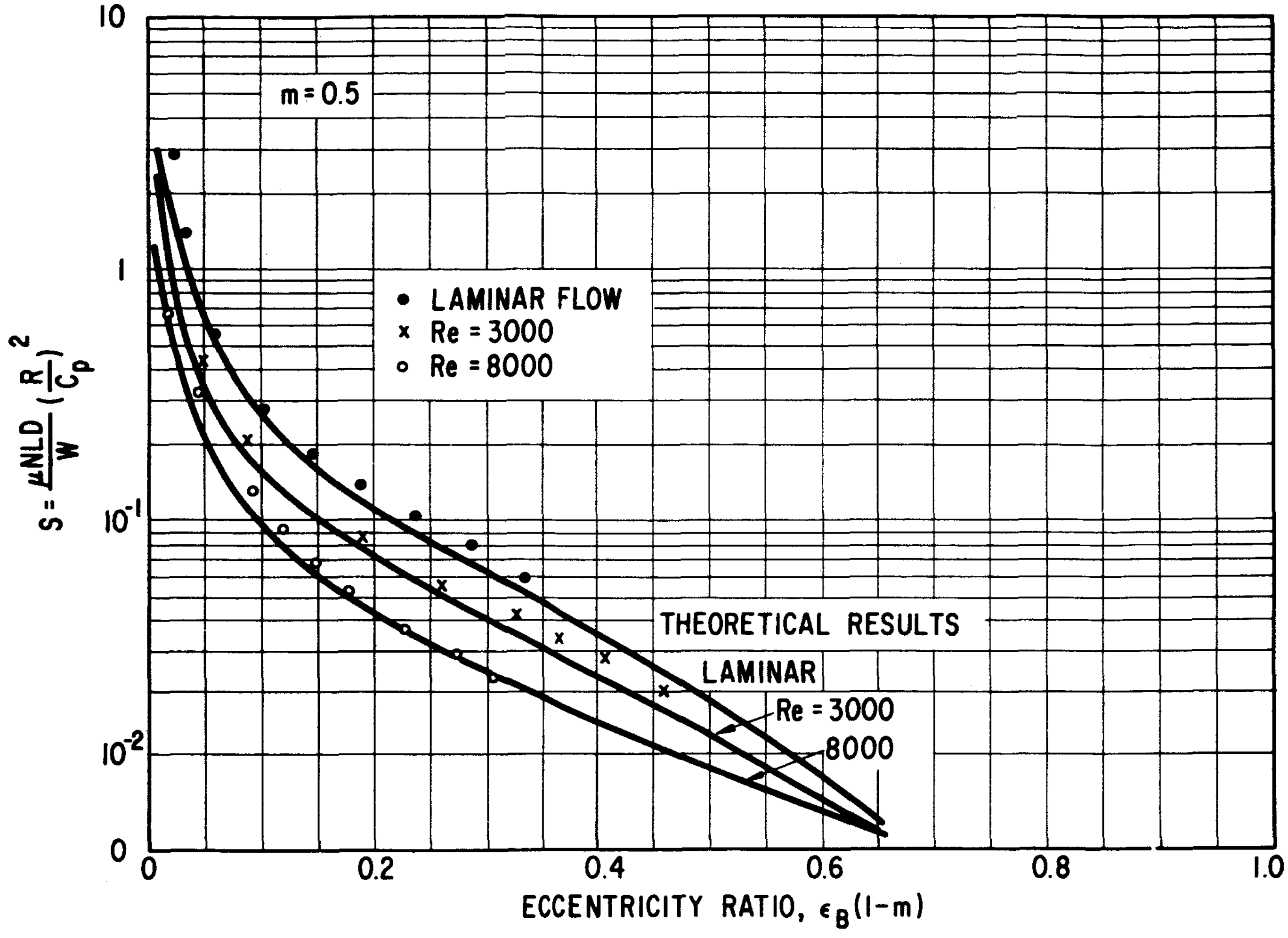

Fig. 9 Tilting-Pad Bearing Static Load Capacity Measurements m = 0.5

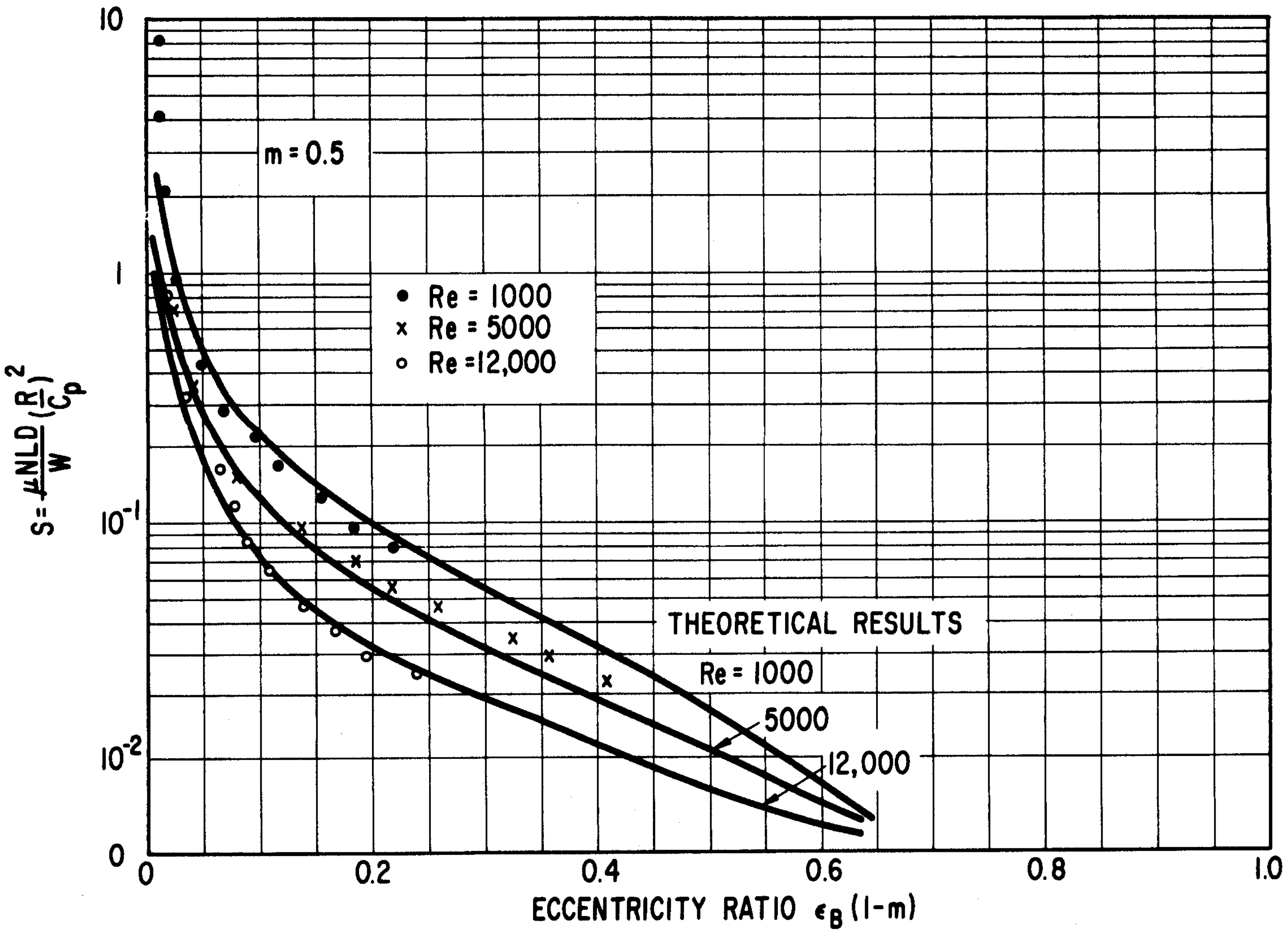

Fig. 10 Tilting-Pad Bearing Static Load Capacity Measurements
m = 0.5

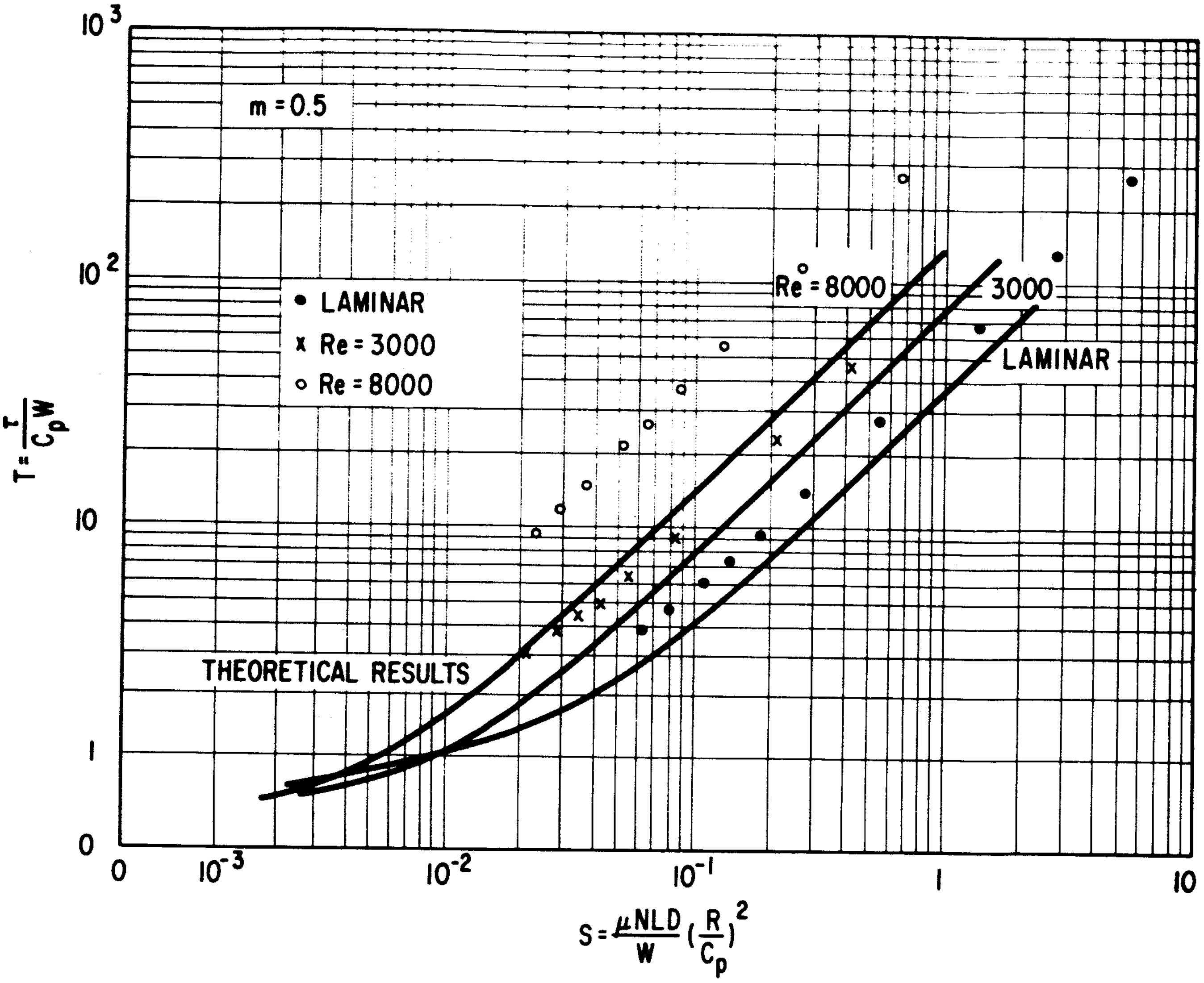

Fig. 11 Tilting-Pad Bearing Measured Friction Torque
m = 0.5

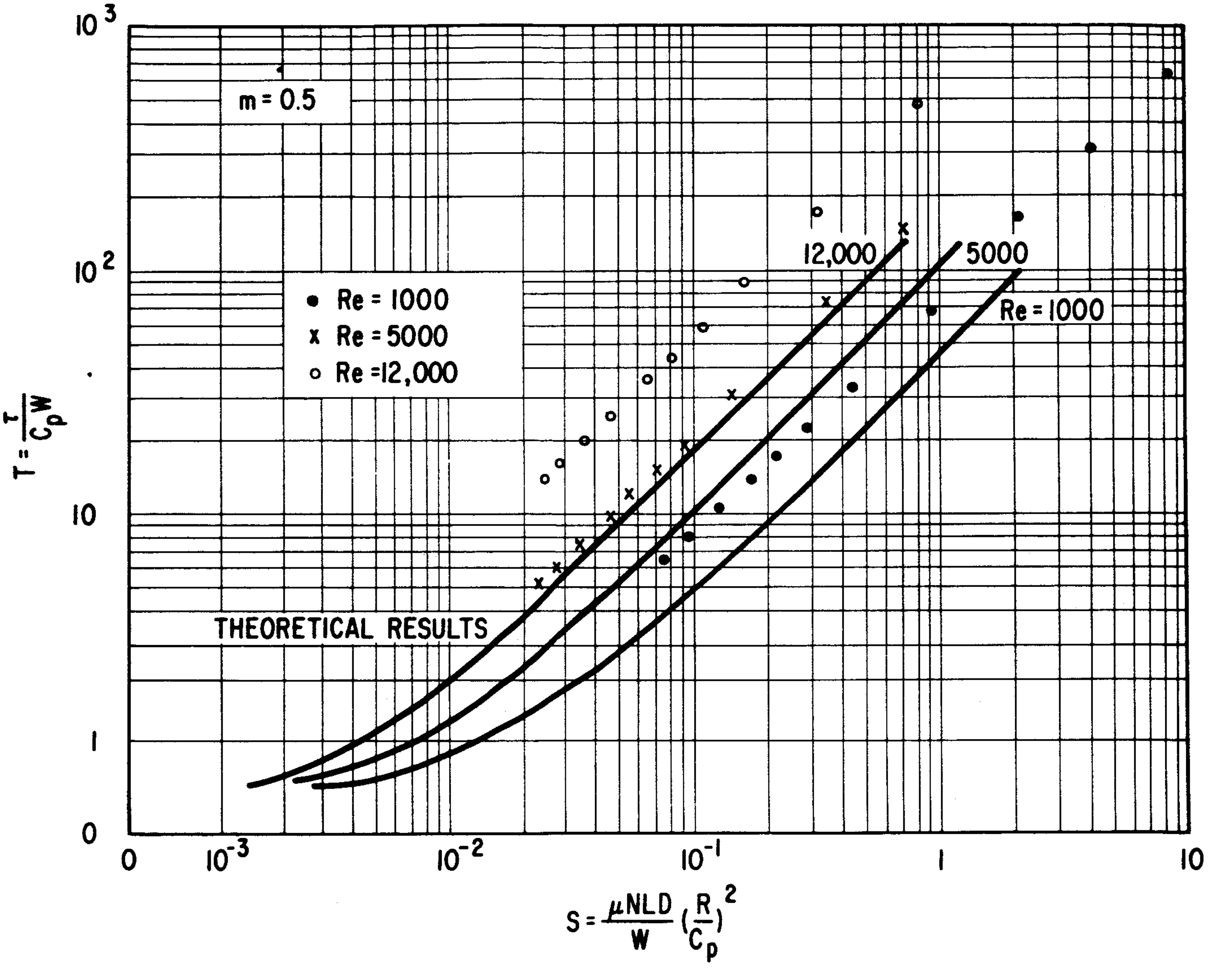

Fig. 12 Tilting-Pad Bearing Measured Friction Torque
m = 0.5

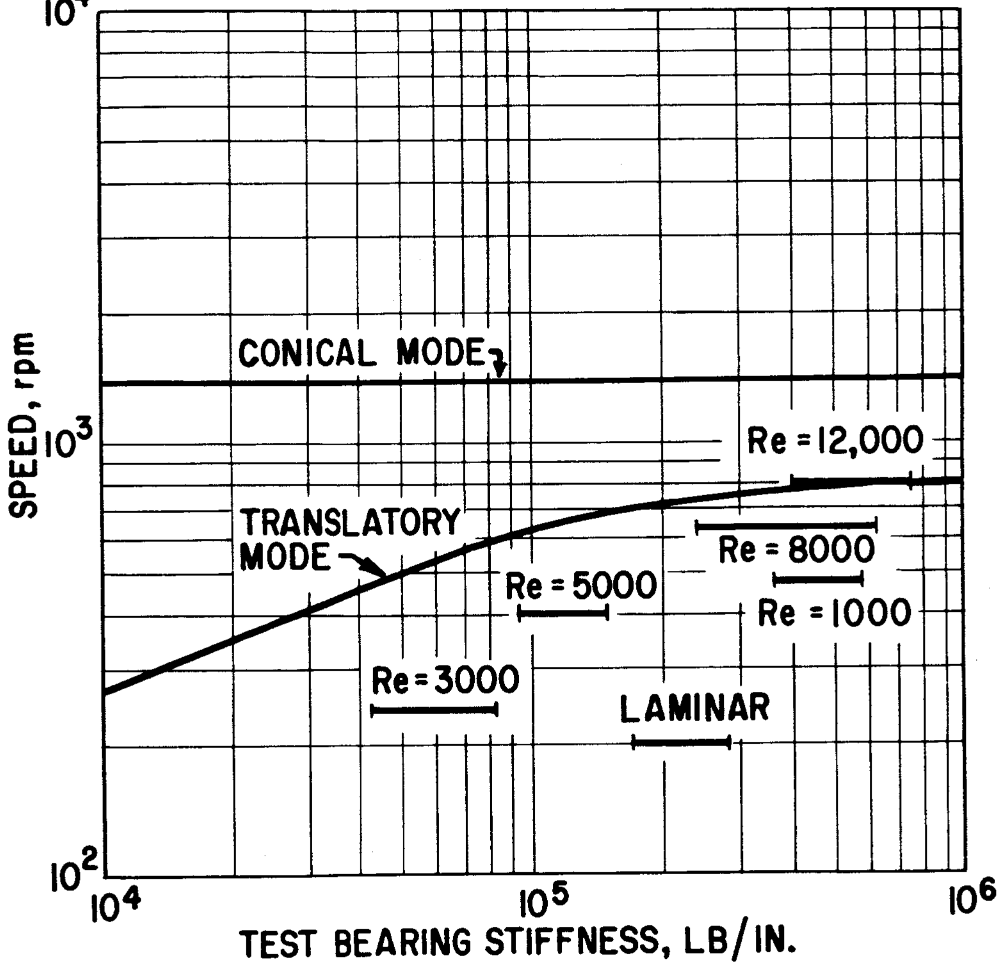

Fig. 13 Critical Speed Map for Dynamic-Load Bearing Apparatus

1. Range of calculated test bearing stiffnesses for the experimental testing (m = 0.5) is given for each Reynolds Number.
2. Support bearing stiffness is constant at 1.3×10^6 lb/in.

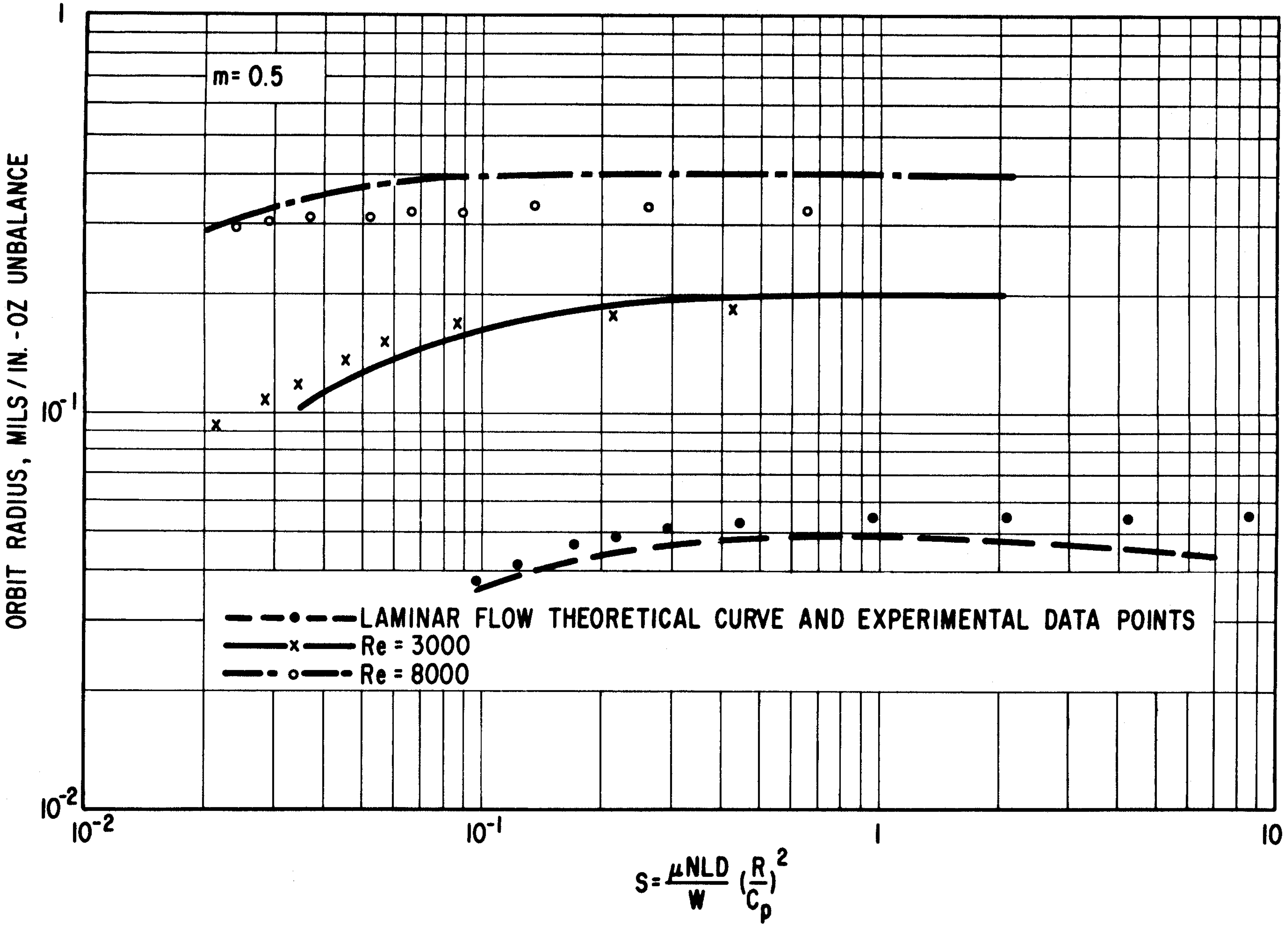

Fig. 14 Tilting-Pad Bearing Dynamic Response Amplitude
m = 0.5

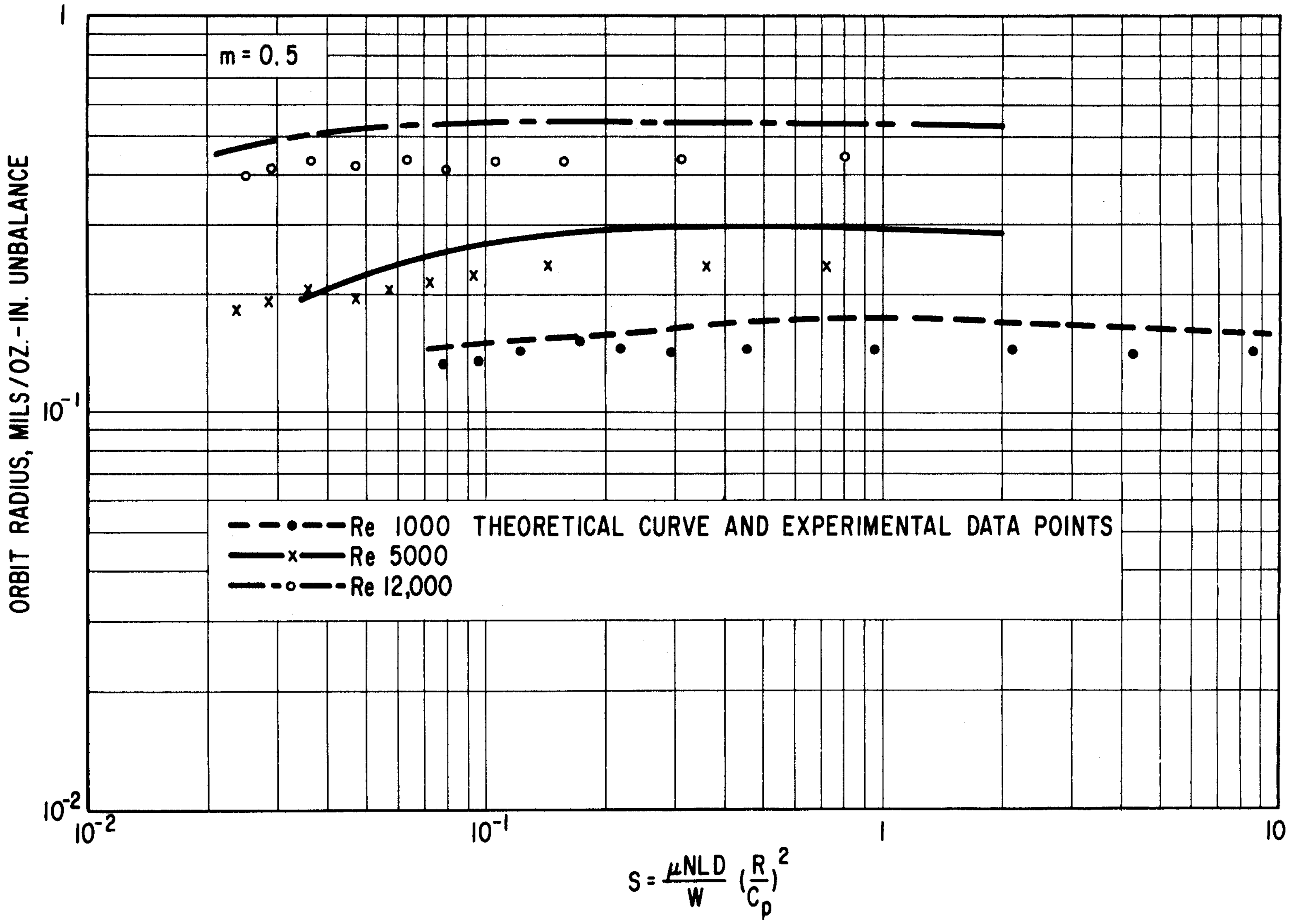

Fig. 15 Tilting-Pad Bearing Dynamic Response Amplitude
m = 0.5

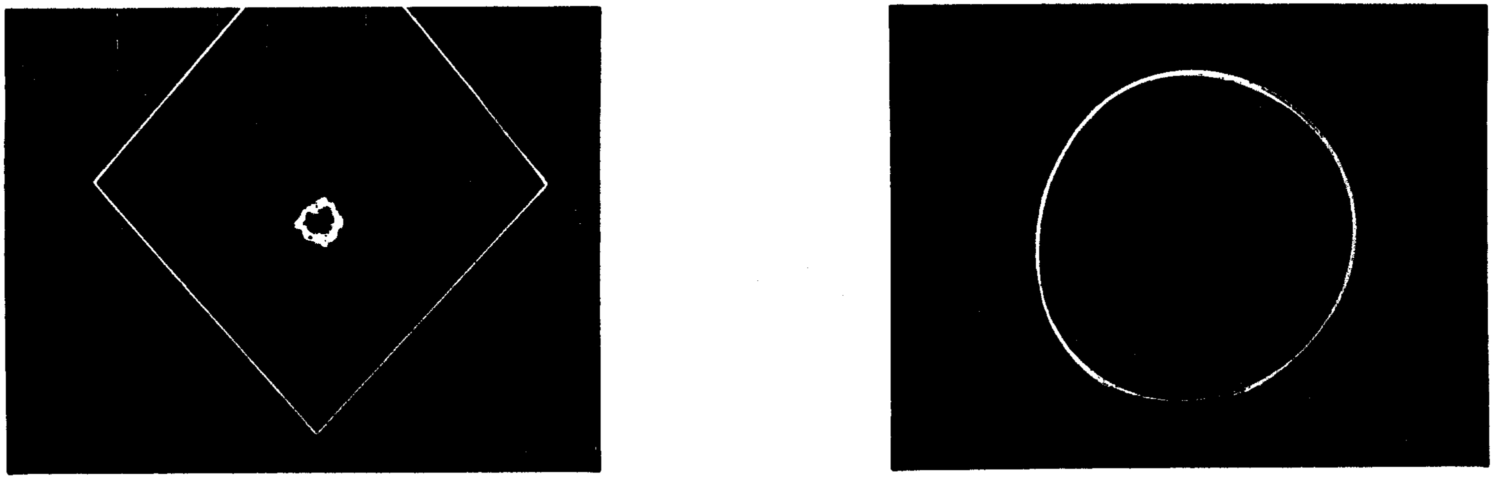

a) DC Coupling, .5 v/cm

b) Filtered, 20 mv/cm

Shaft Displacement at Test Bearing - 4000 rpm (Re = 5000), 50 lb. load

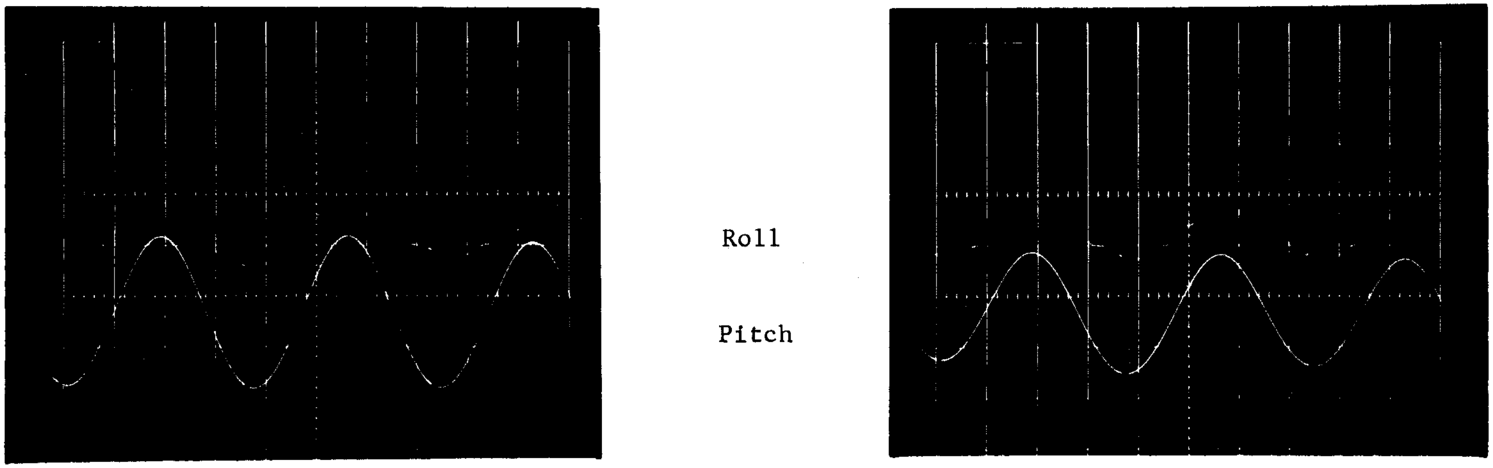

c) 50 lb. load, 10 mv/cm 2.5 msec/cm

d) 250 lb. load, 10 mv/cm, 2.5 msec/cm

Roll and Pitch Motions of Bearing Pad - 6400 rpm (Re = 8000)

Fig. 16 Oscilloscope Traces of Tilting-Pad Bearing Shaft and Pad Motions

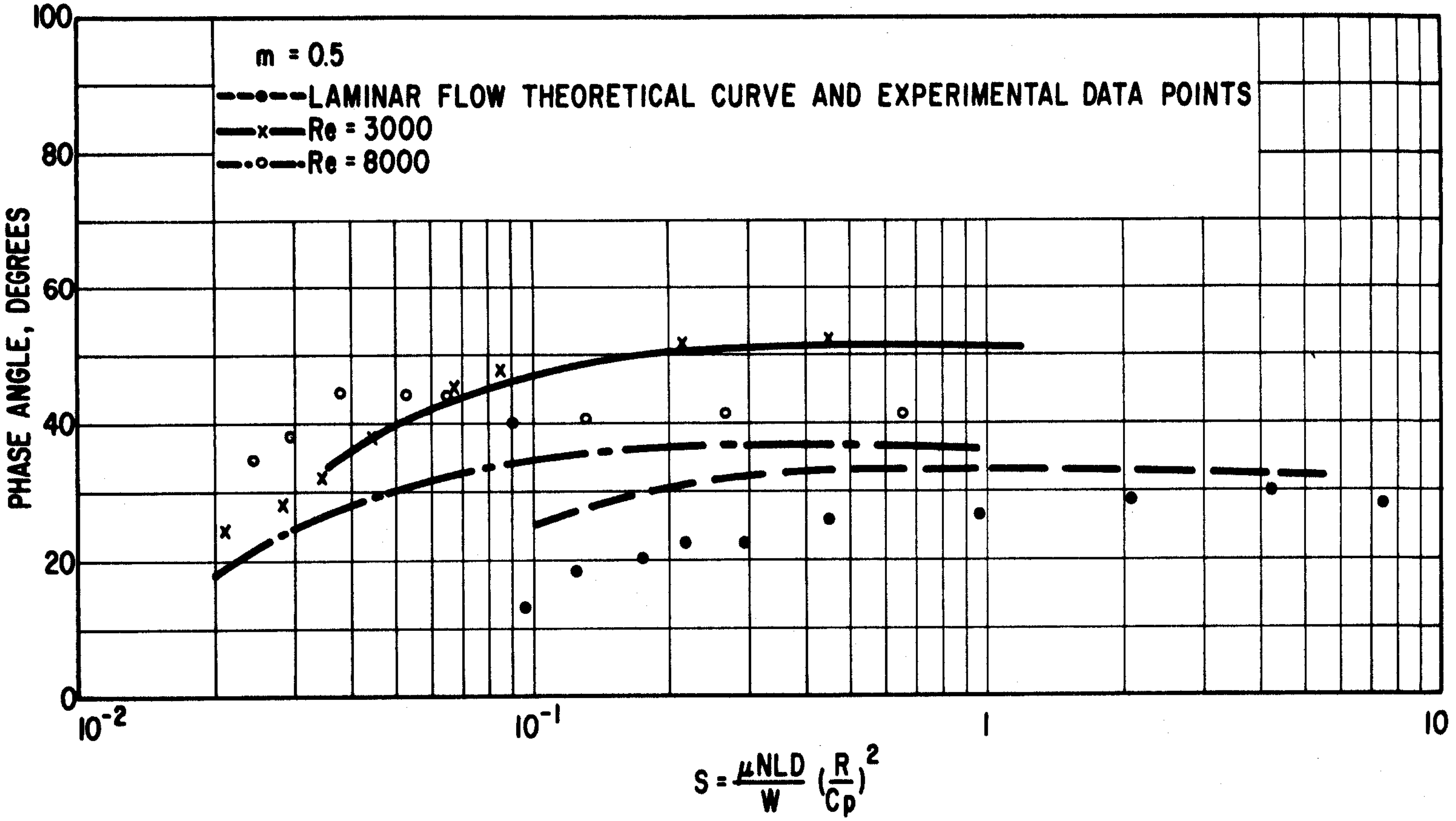

Fig. 17 Tilting-Pad Bearing Dynamic Response Phase Angle

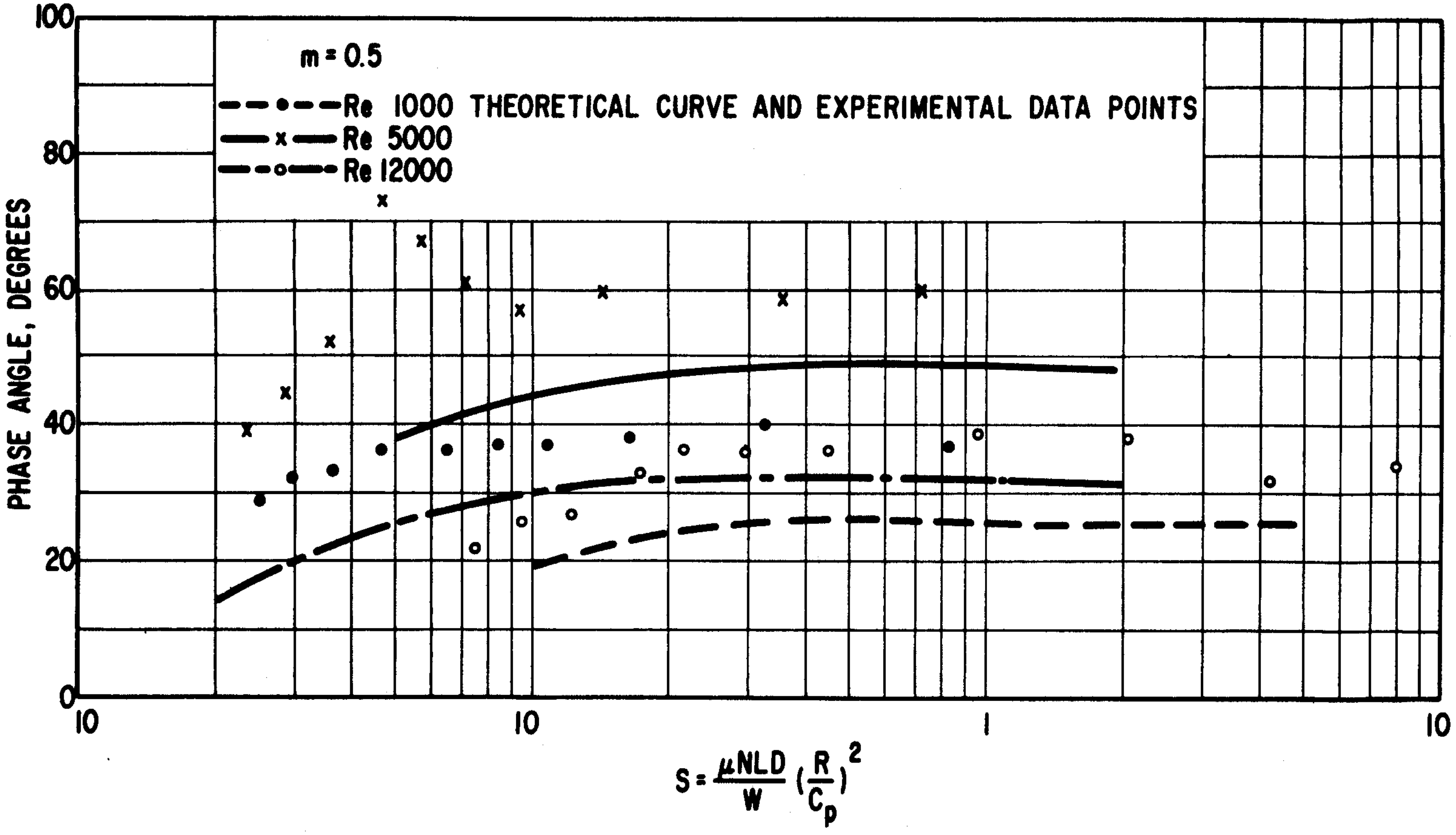

Fig. 18 Tilting-Pad Bearing Dynamic Response Phase Angle

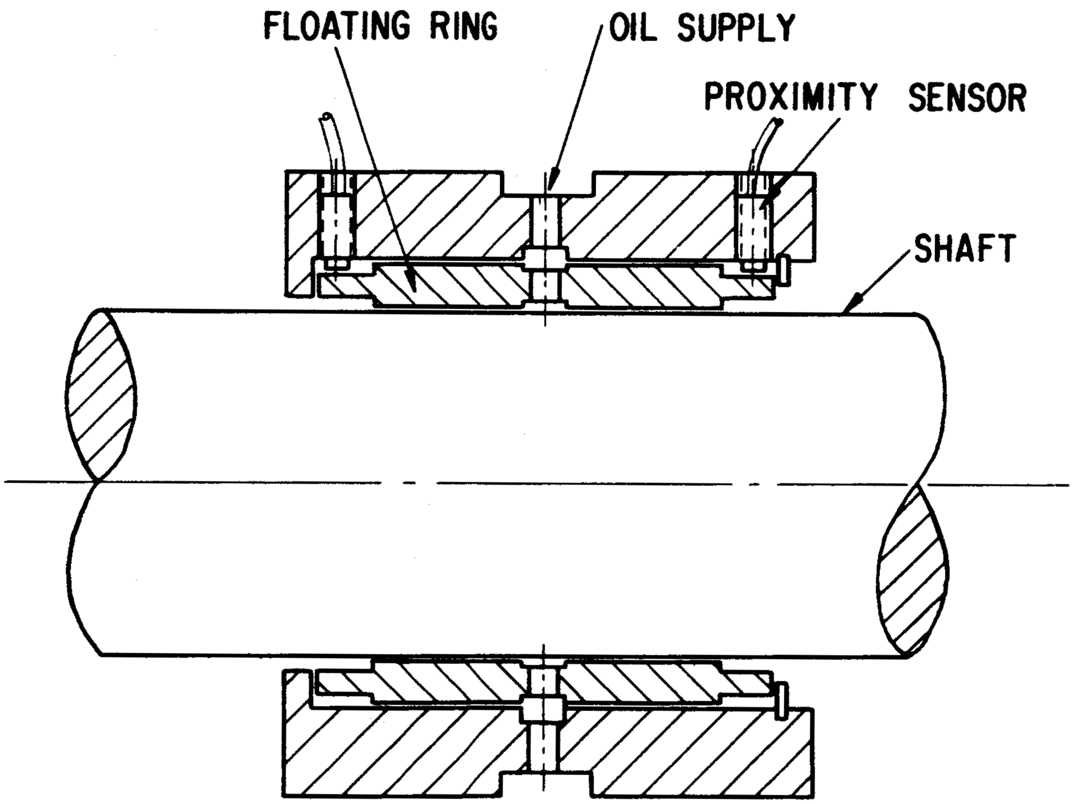
FLOATING RING
OIL SUPPLY
PROXIMITY SENSOR
SHAFT

Fig. 19 Schematic of Floating-Ring Bearing

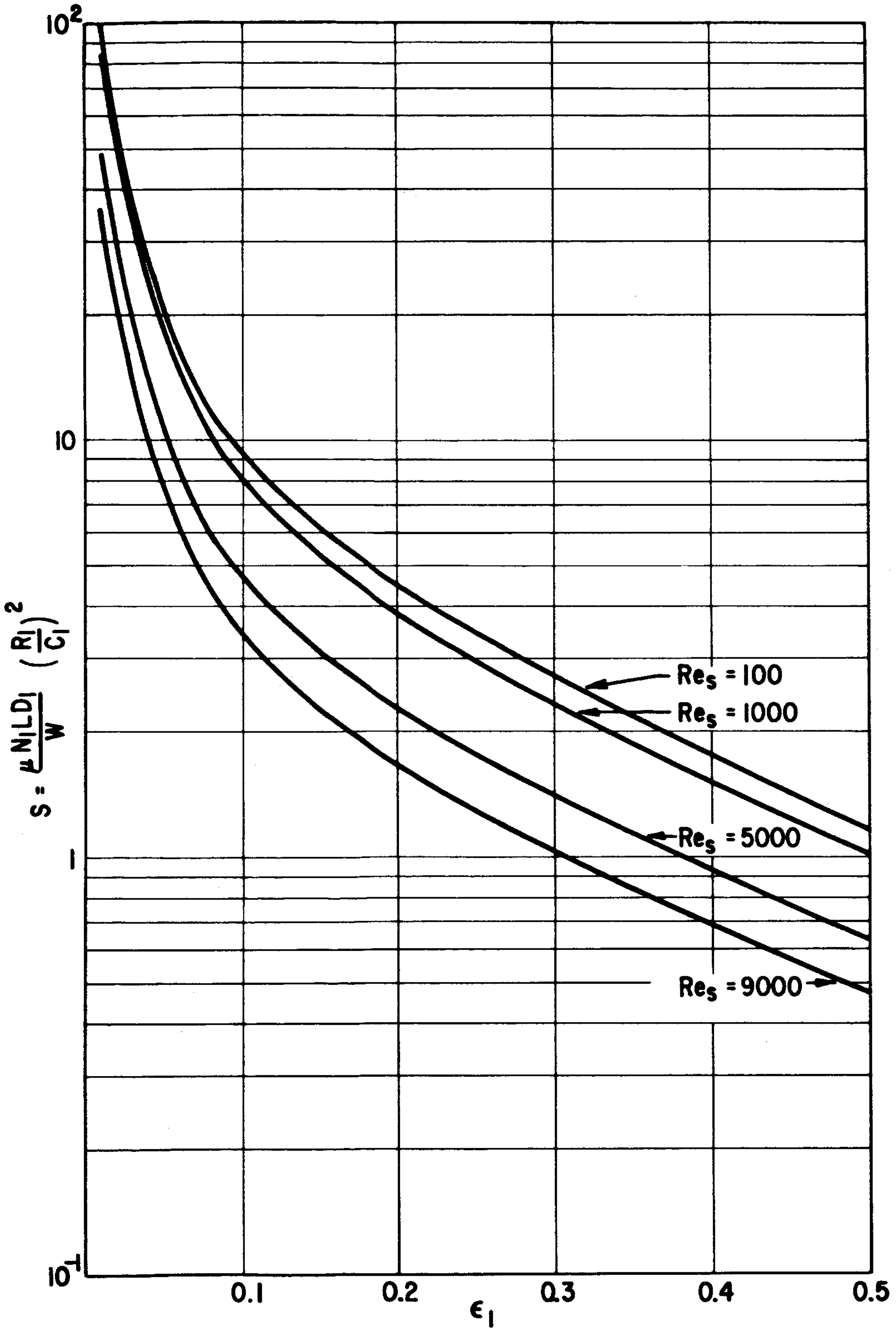

Fig. 20 Floating-Ring Bearing — Inner Film Static Load Capacity $C_2/C_1 = 0.7$, $P_s L D_1/W = 0.2$

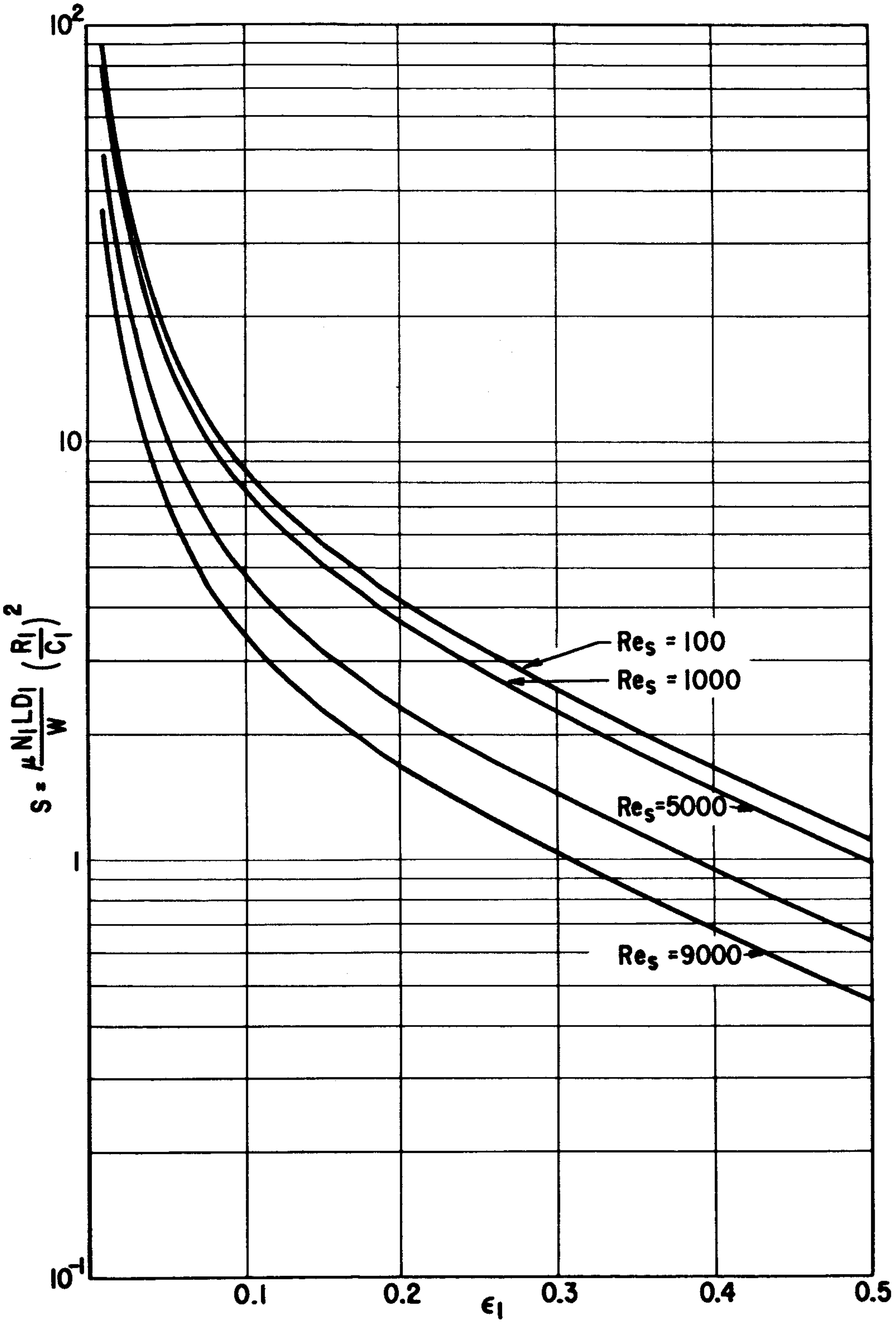

Fig. 21 Floating-Ring Bearing — Inner Film Static Load Capacity $C_2/C_1 = 1.3$, $P_s L D_1/W = 0.2$

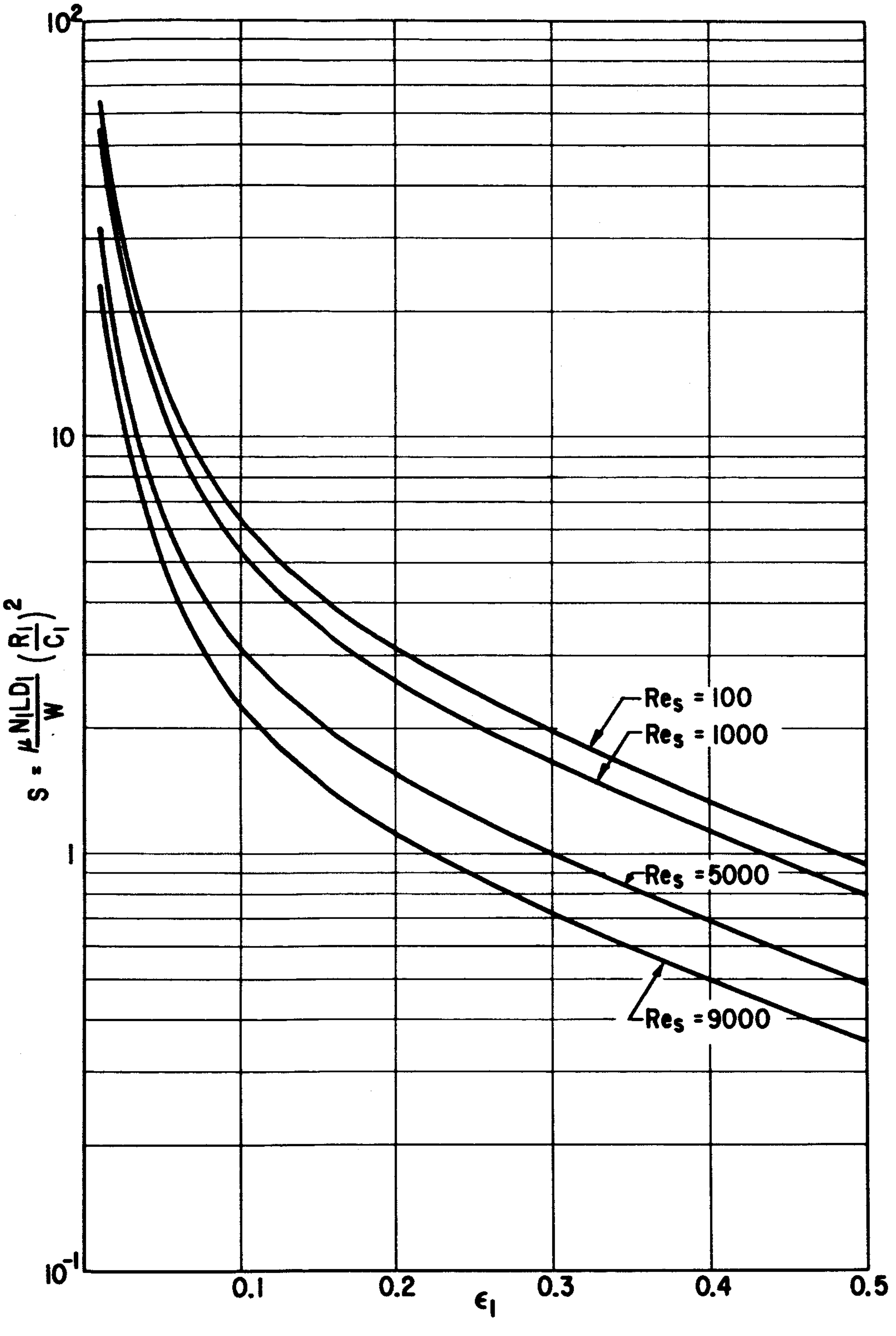

Fig. 22 Floating-Ring Bearing — Inner Film Static Load Capacity $C_2/C_1 = 0.7$, $P_sLD_1/W = 1.5$

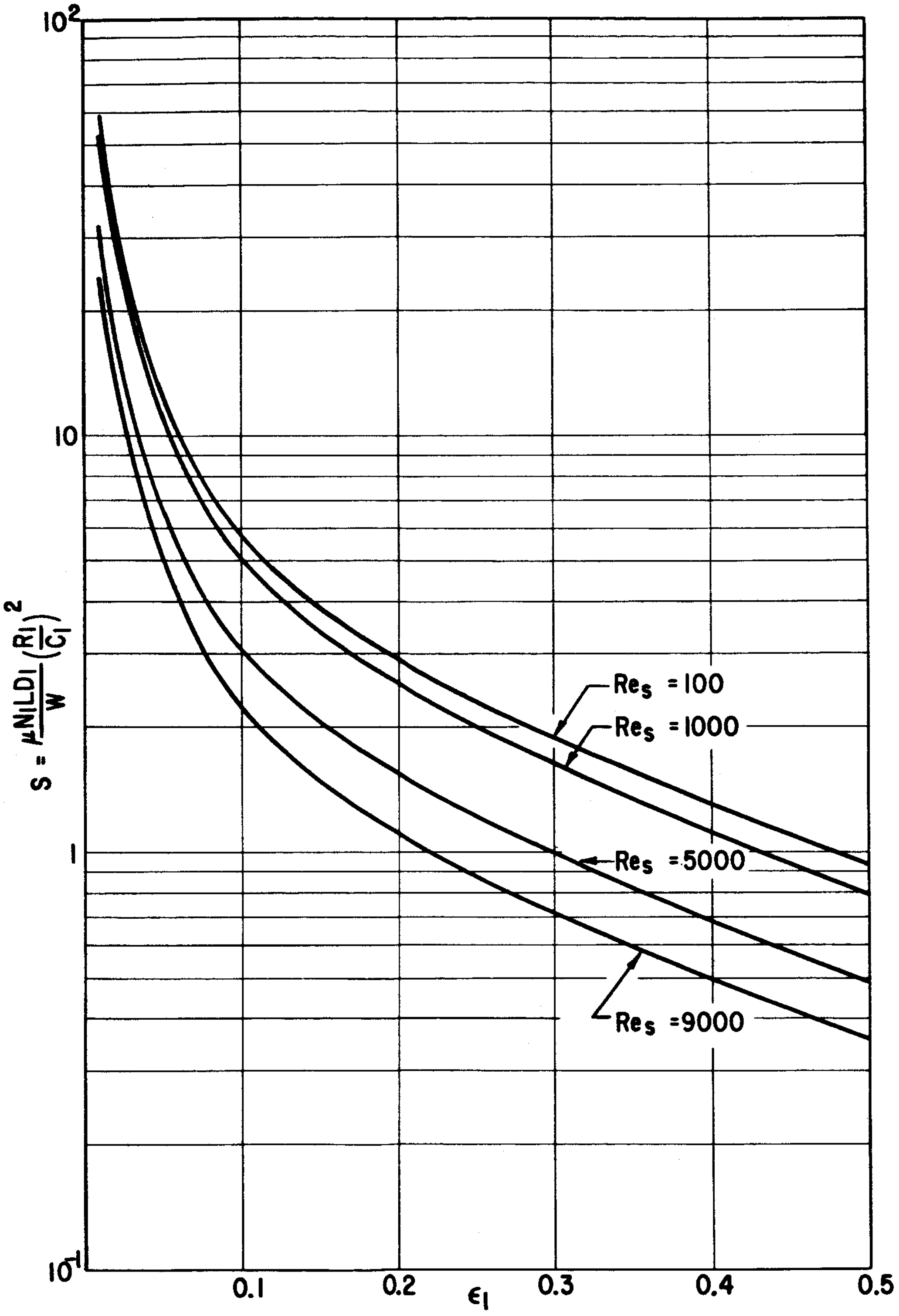

Fig. 23 Floating-Ring Bearing — Inner Film Static Load Capacity
$C_2/C_1 = 1.3$, $P_sLD_1/W = 1.5$

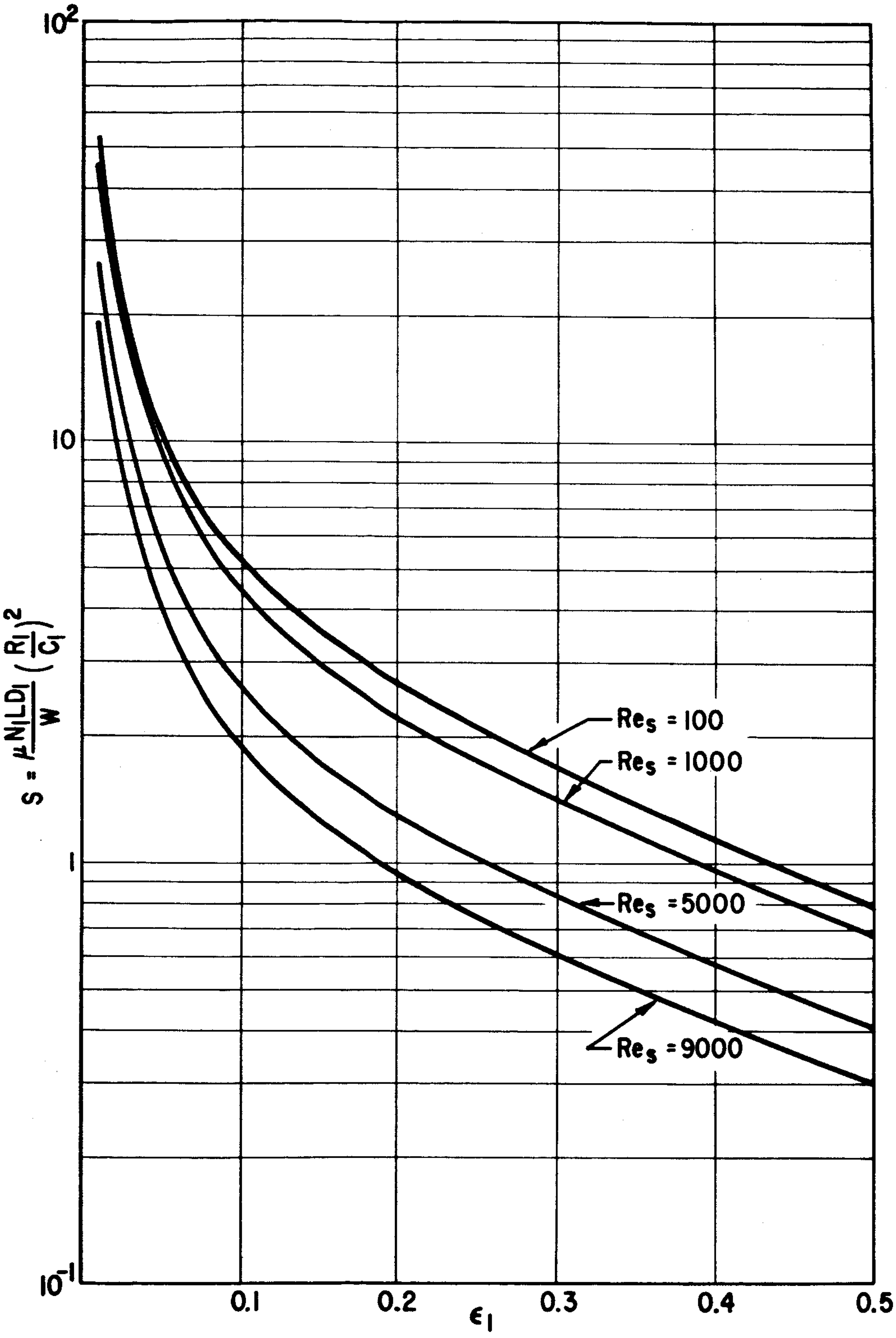

Fig. 24 Floating-Ring Bearing — Inner Film Static Load Capacity $C_2/C_1 = 0.7$, $P_s L D_1/W = 10.0$

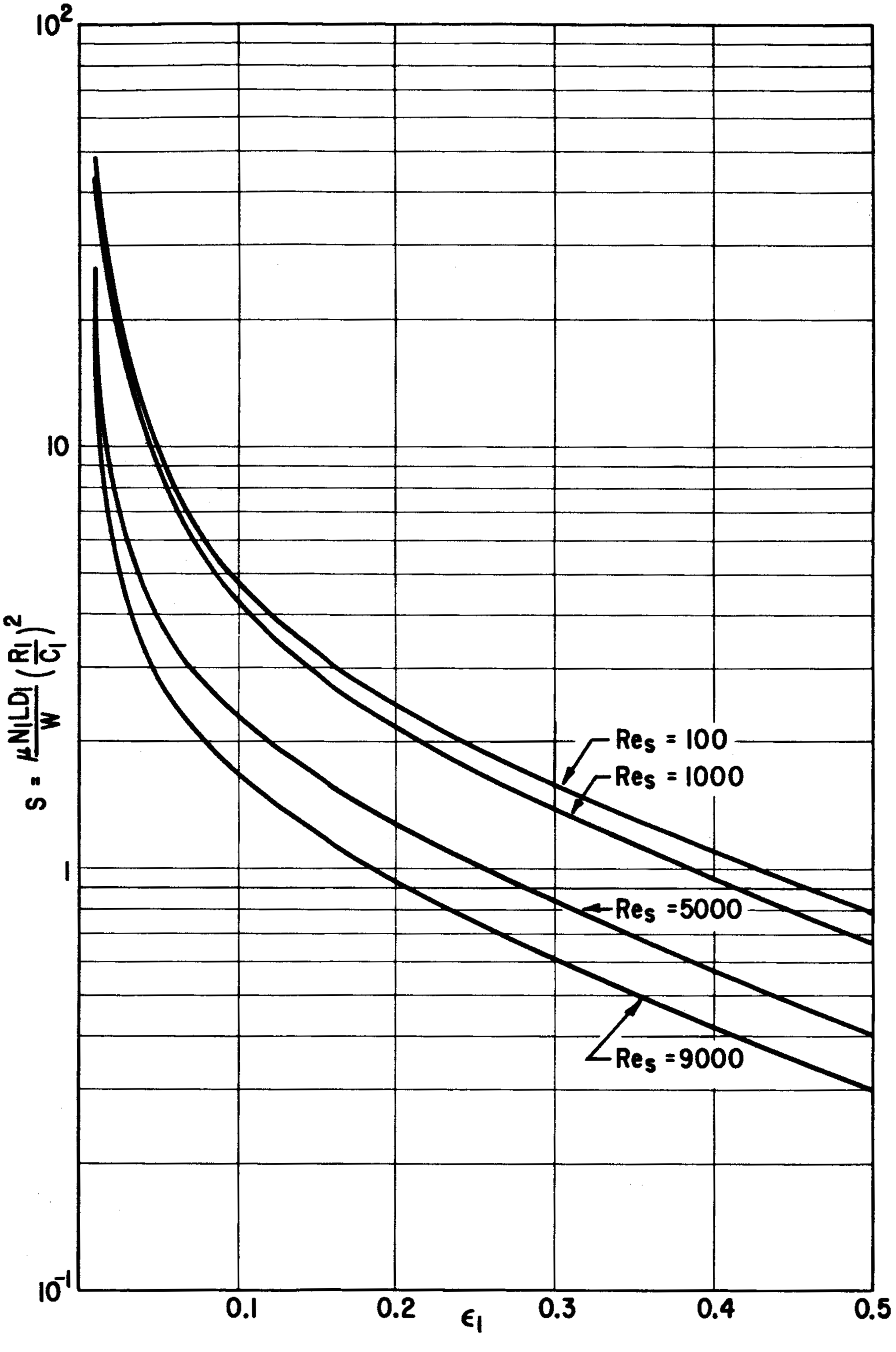

Fig. 25 Floating-Ring Bearing — Inner Film Static Load Capacity $C_2/C_1 = 1.3$, $P_s LD_1/W = 10.0$

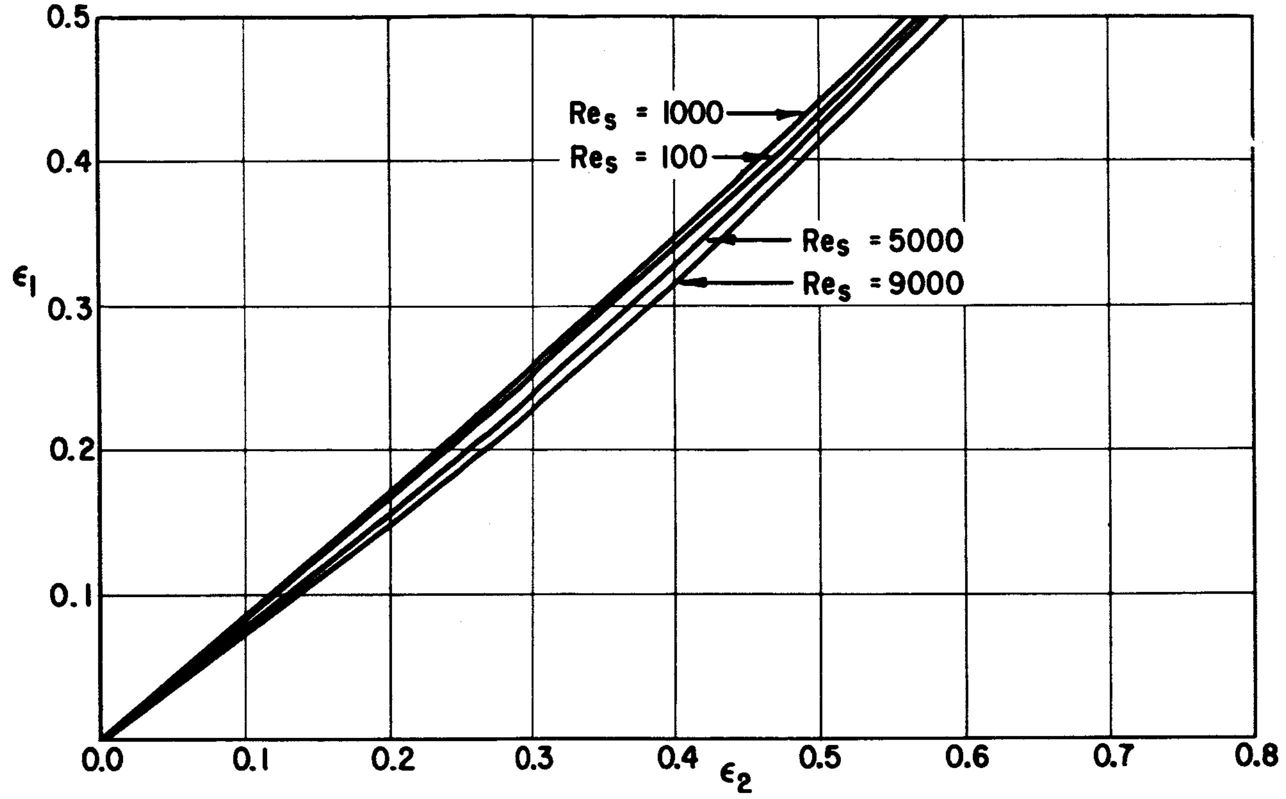

Fig. 26 Relationship Between Inner and Outer Film Eccentricity Ratios $C_2/C_1 = 0.7$, $P_s LD_1/W = 0.2$

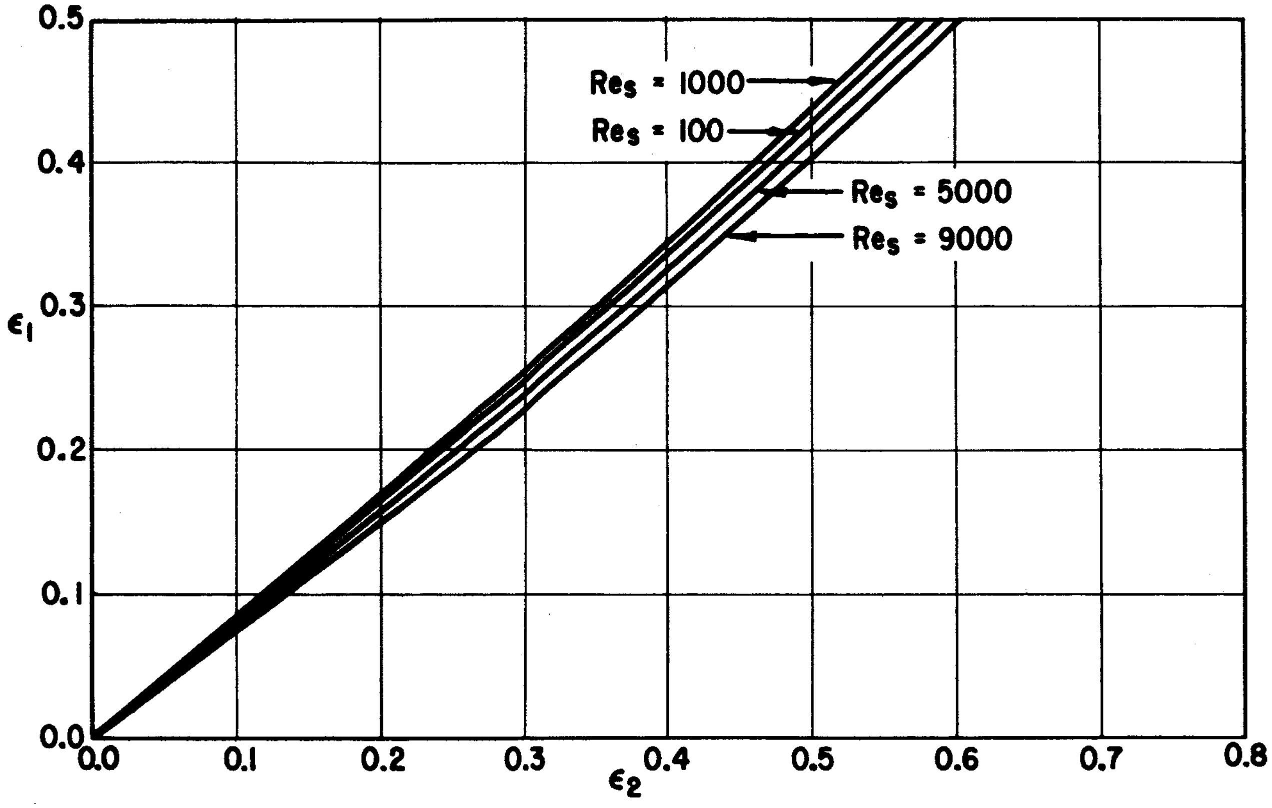

Fig. 27 Relationship Between Inner and Outer Film Eccentricity Ratios $C_2/C_1 = 0.7$, $P_s LD_1/W = 1.5$

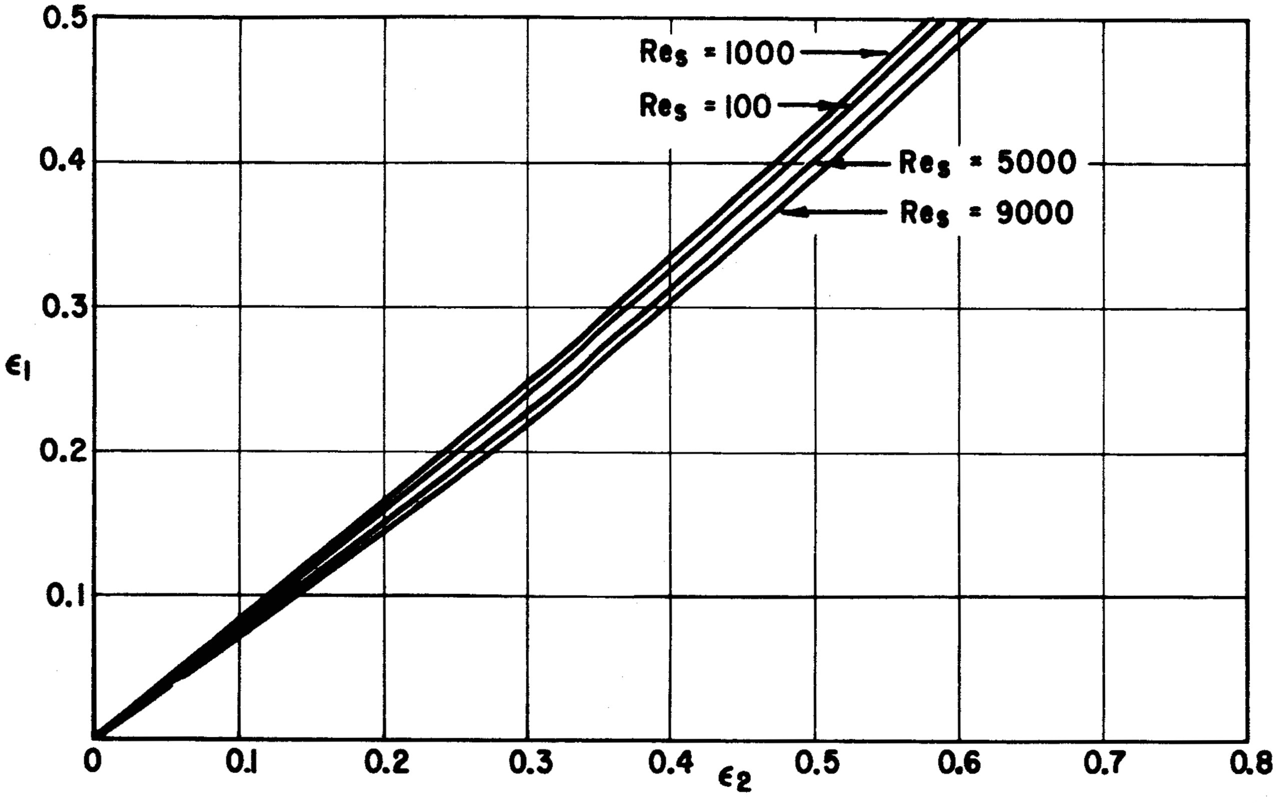

Fig. 28 Relationship Between Inner and Outer Film Eccentricity Ratios $C_2/C_1 = 0.7$, $P_sLD_1/W = 10.0$

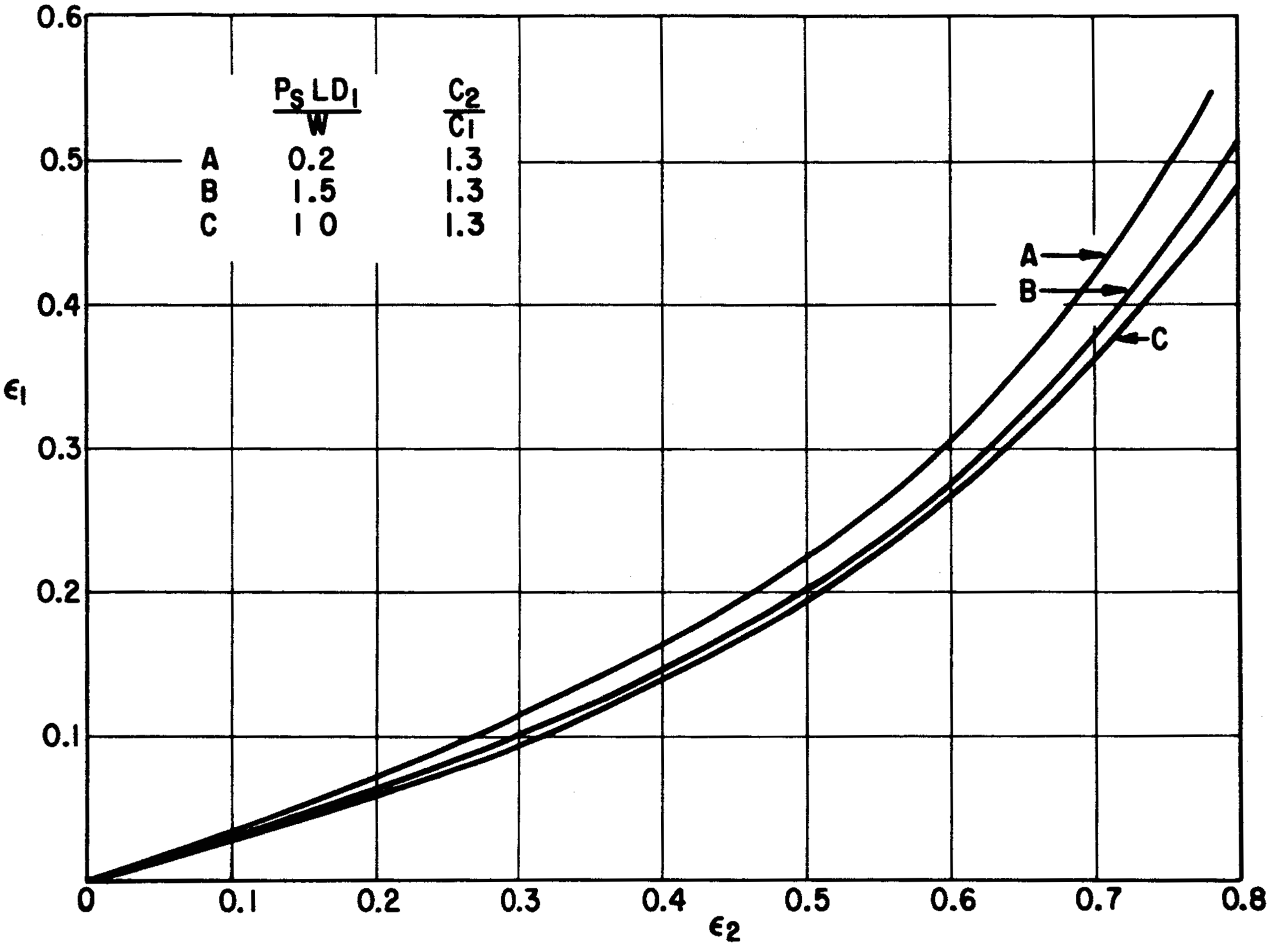

Fig. 29 Relationship Between Inner and Outer Film Eccentricity Ratios $C_2/C_1 = 1.3$. The effect of Reynolds Number is negligible.

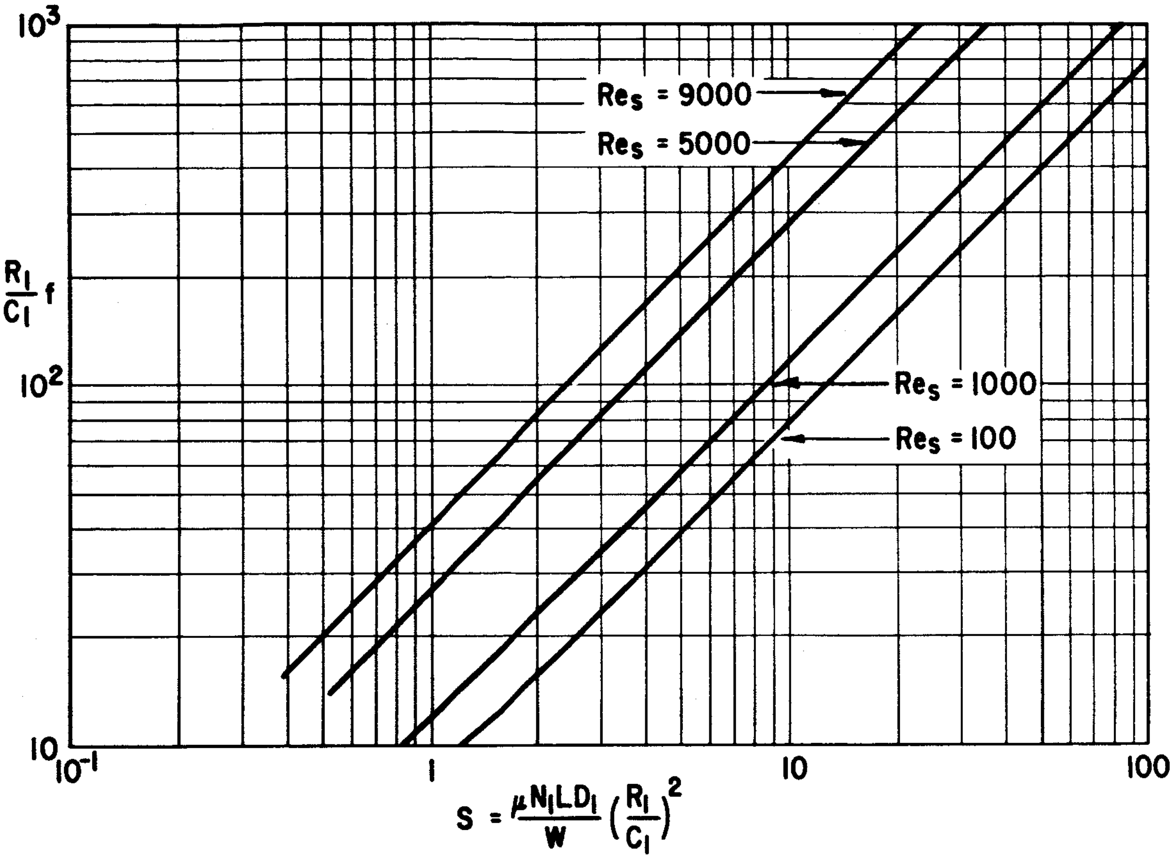

Fig. 30 Floating-Ring Bearing Friction Factor
$C_2/C_1 = 0.7$, $P_s L D_1/W = 0.2$

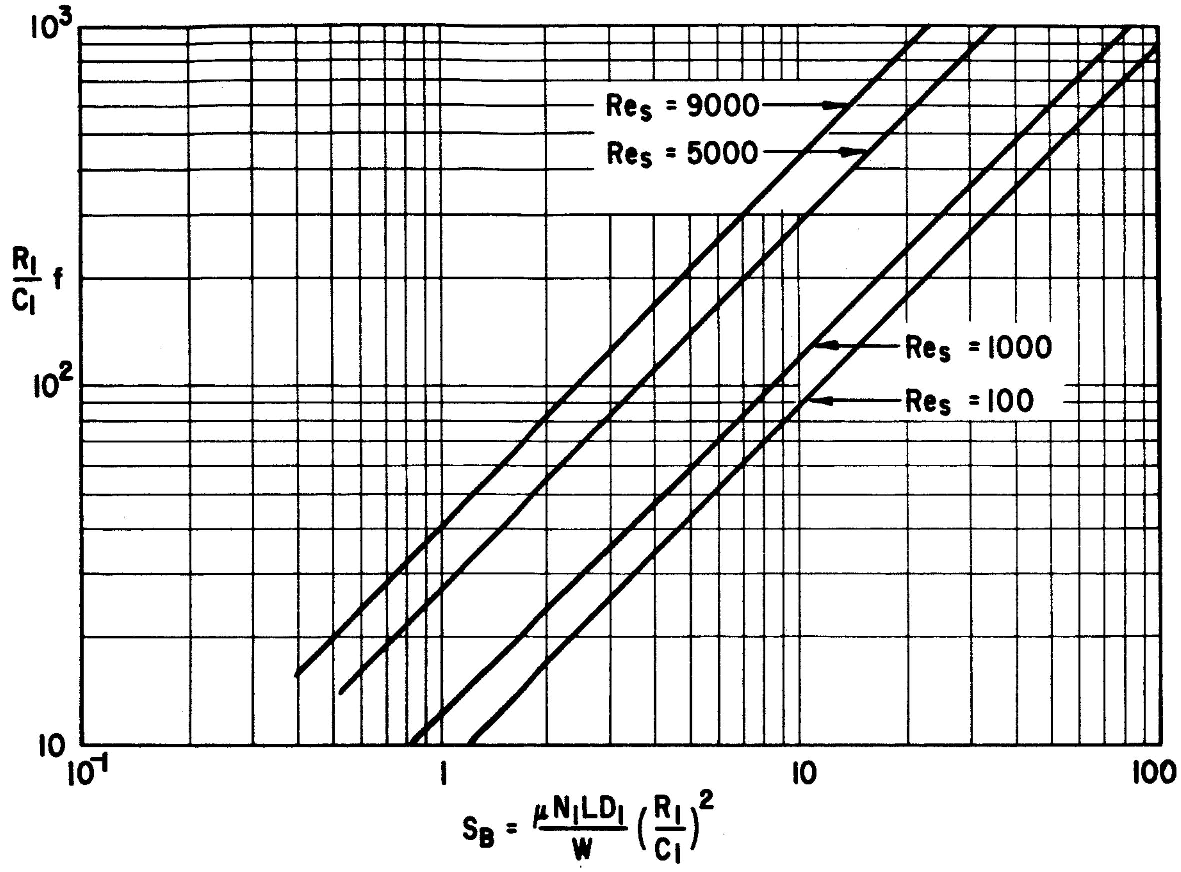

Fig. 31 Floating-Ring Bearing Friction Factor
$C_2/C_1 = 1.3$, $P_s L D_1/W = 0.2$

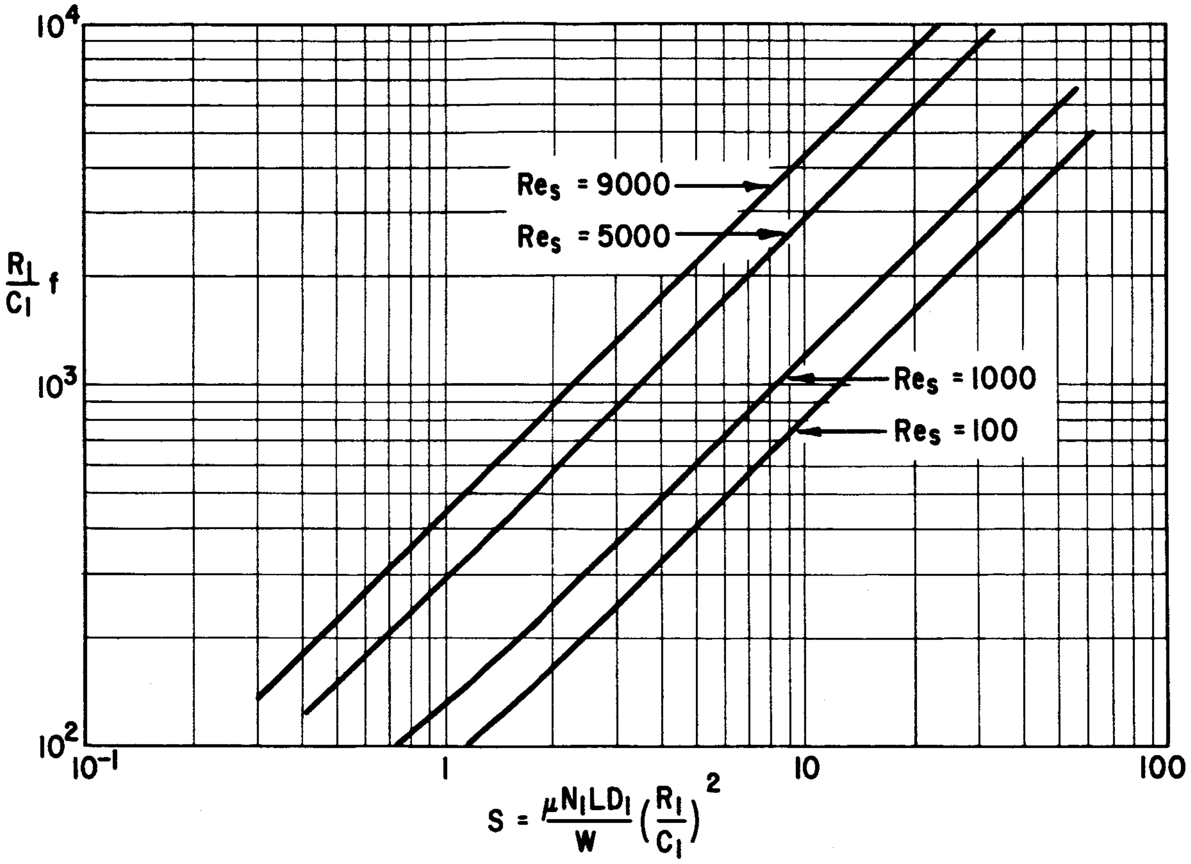

Fig. 32 Floating-Ring Bearing Friction Factor
$C_2/C_1 = 0.7$, $P_s L D_1/W = 1.5$

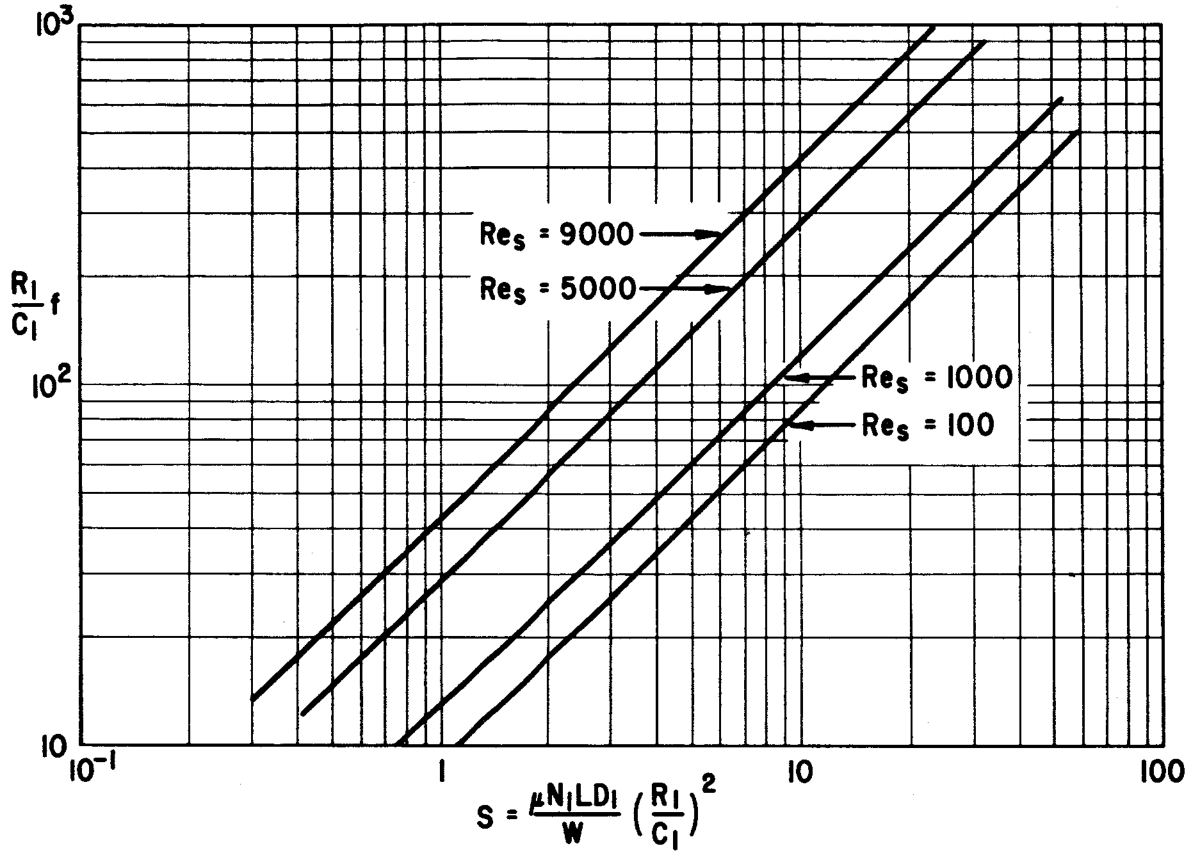

Fig. 33 Floating-Ring Bearing Friction Factor
$C_2/C_1 = 1.3$, $P_s L D_1/W = 1.5$

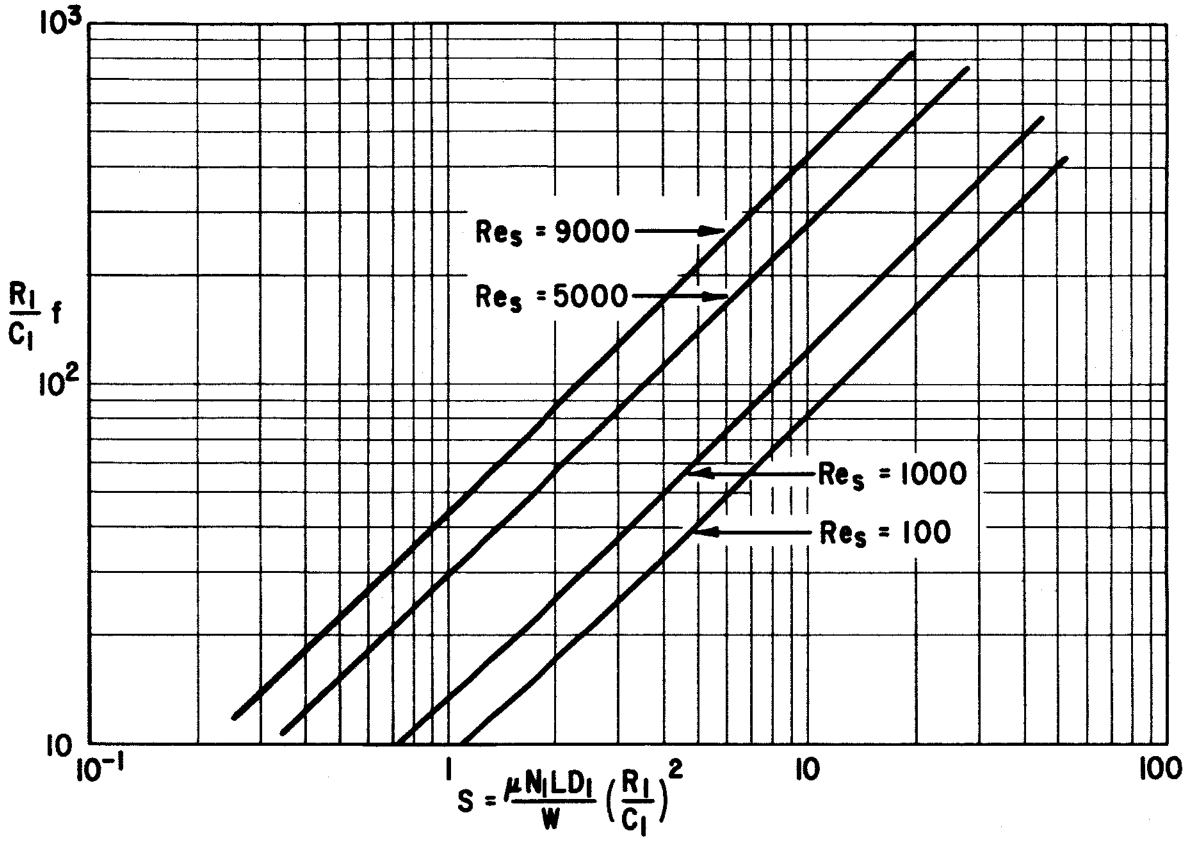

Fig. 34 Floating-Ring Bearing Friction Factor
$C_2/C_1 = 0.7$, $P_s LD_1/W = 10.0$

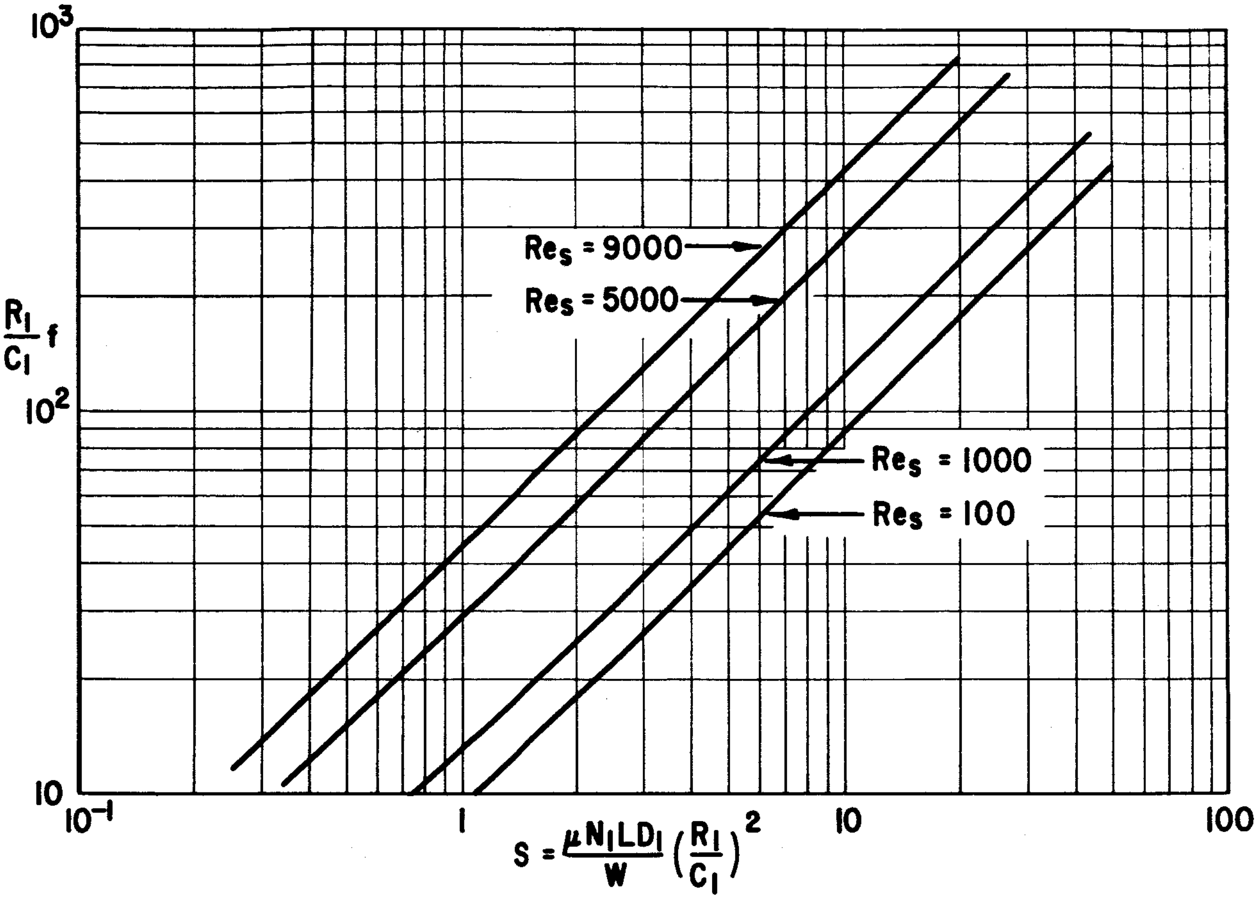

Fig. 35 Floating-Ring Bearing Friction Factor
$C_2/C_1 = 1.3$, $P_s L D_1/W = 10.0$

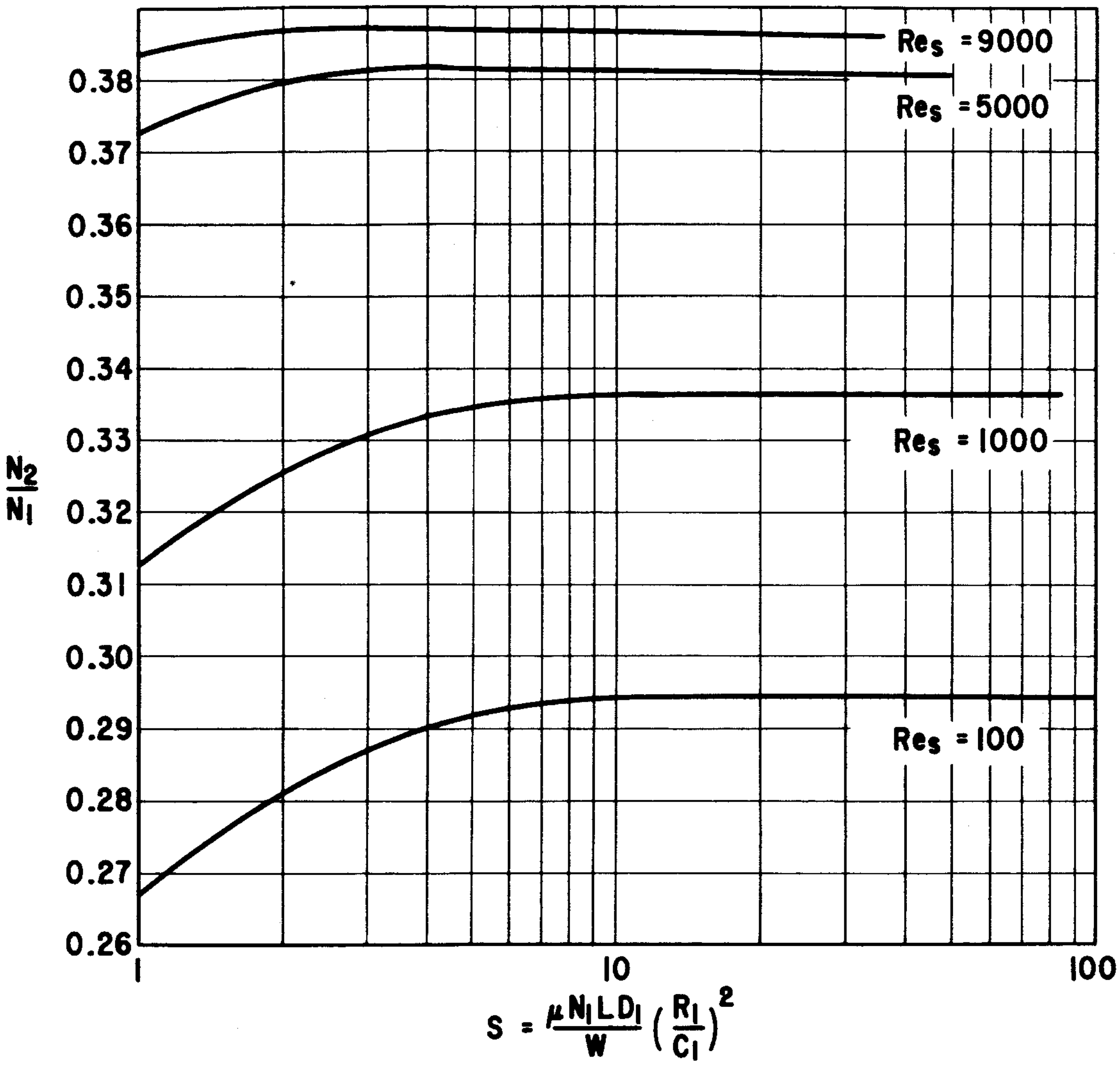

Fig. 36 Floating-Ring Bearing Ring/Shaft Speed Ratio
$C_2/C_1 = 0.7$, $P_s L D_1/W = 0.2$

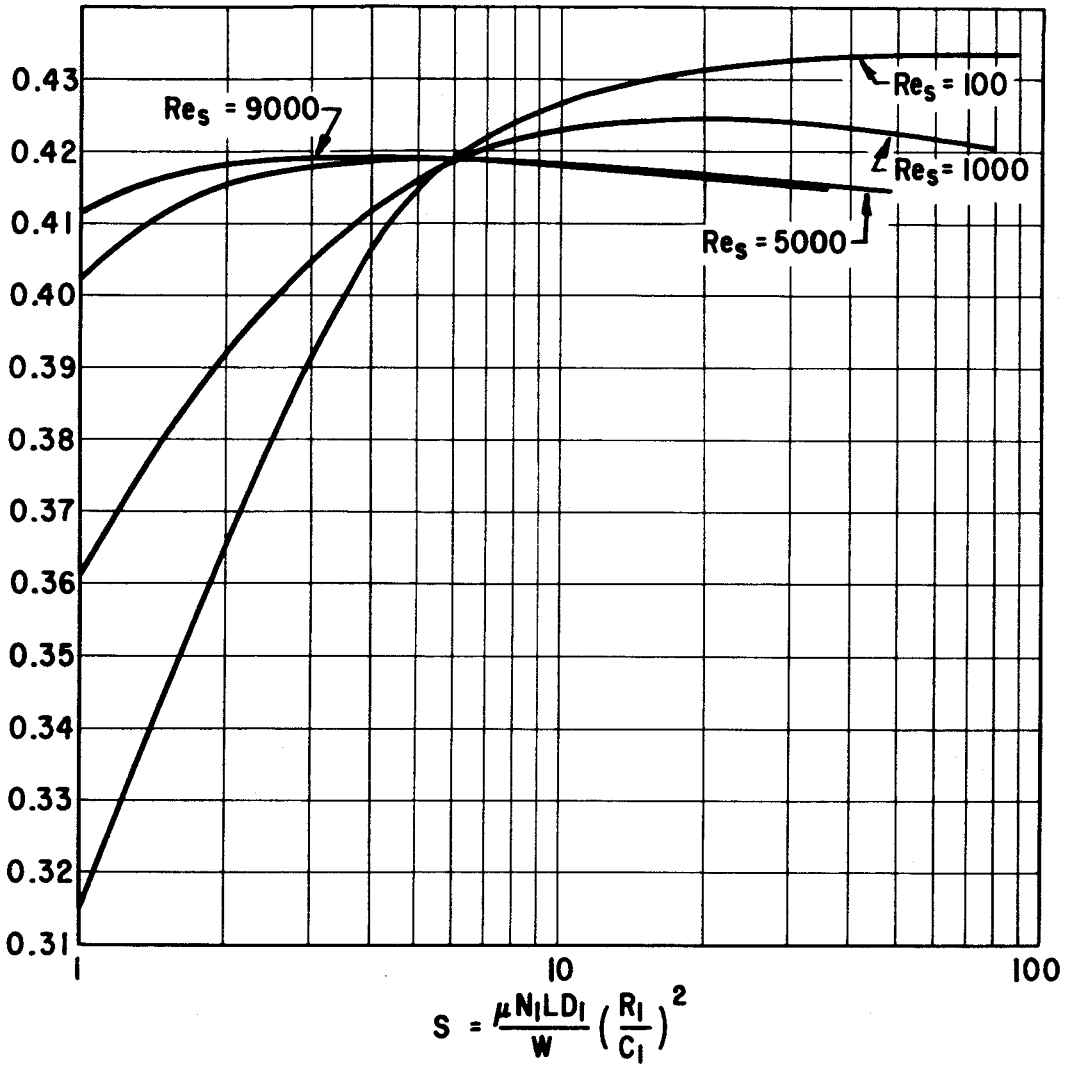

Fig. 37 Floating-Ring Bearing Ring/Shaft Speed Ratio
$C_2/C_1 = 1.3$, $P_s LD_1/W = 0.2$

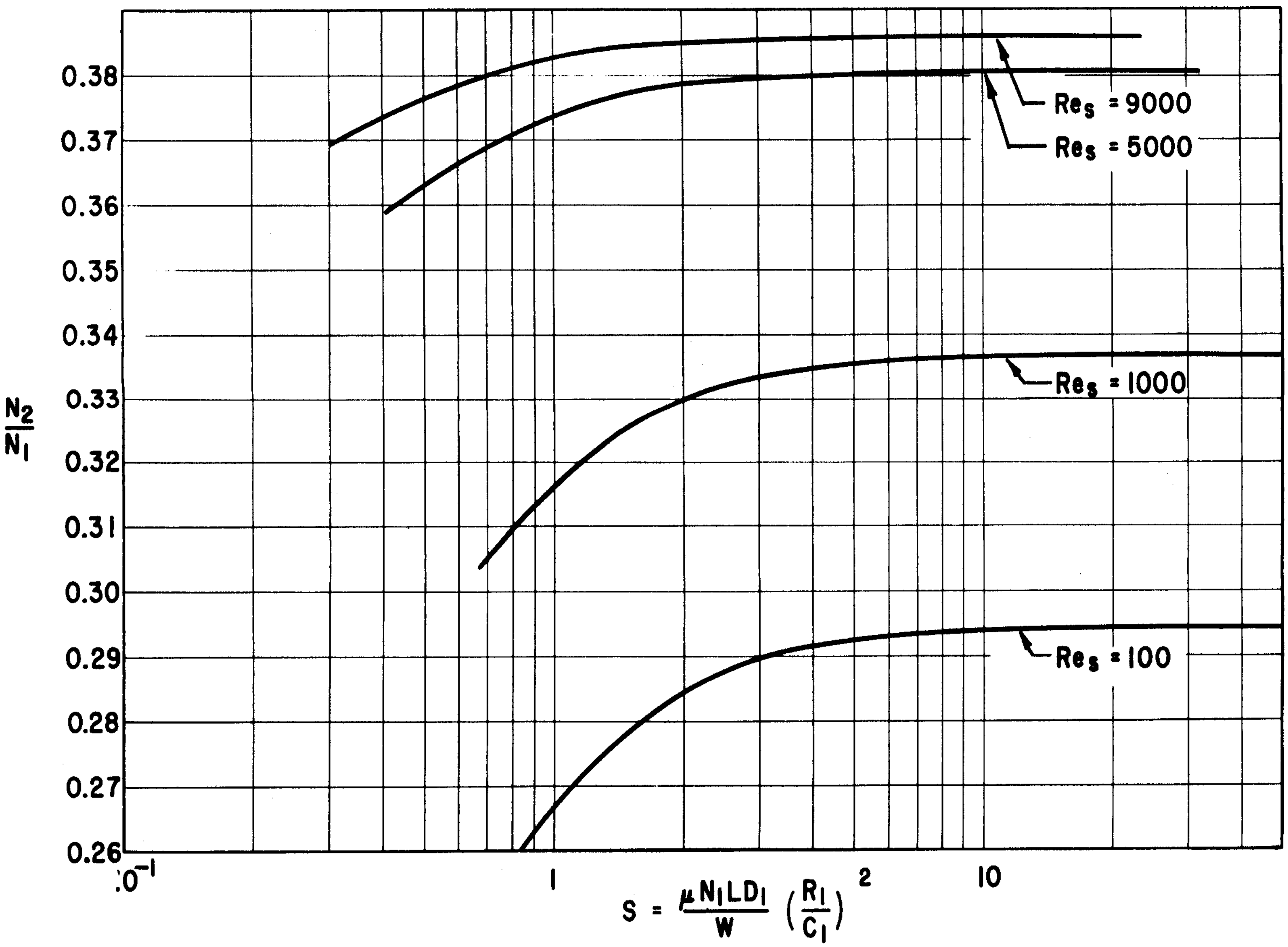

Fig. 38 Floating-Ring Bearing Ring/Shaft Speed Ratio
$C_2/C_1 = 0.7$, $P_s LD_1/W = 1.5$

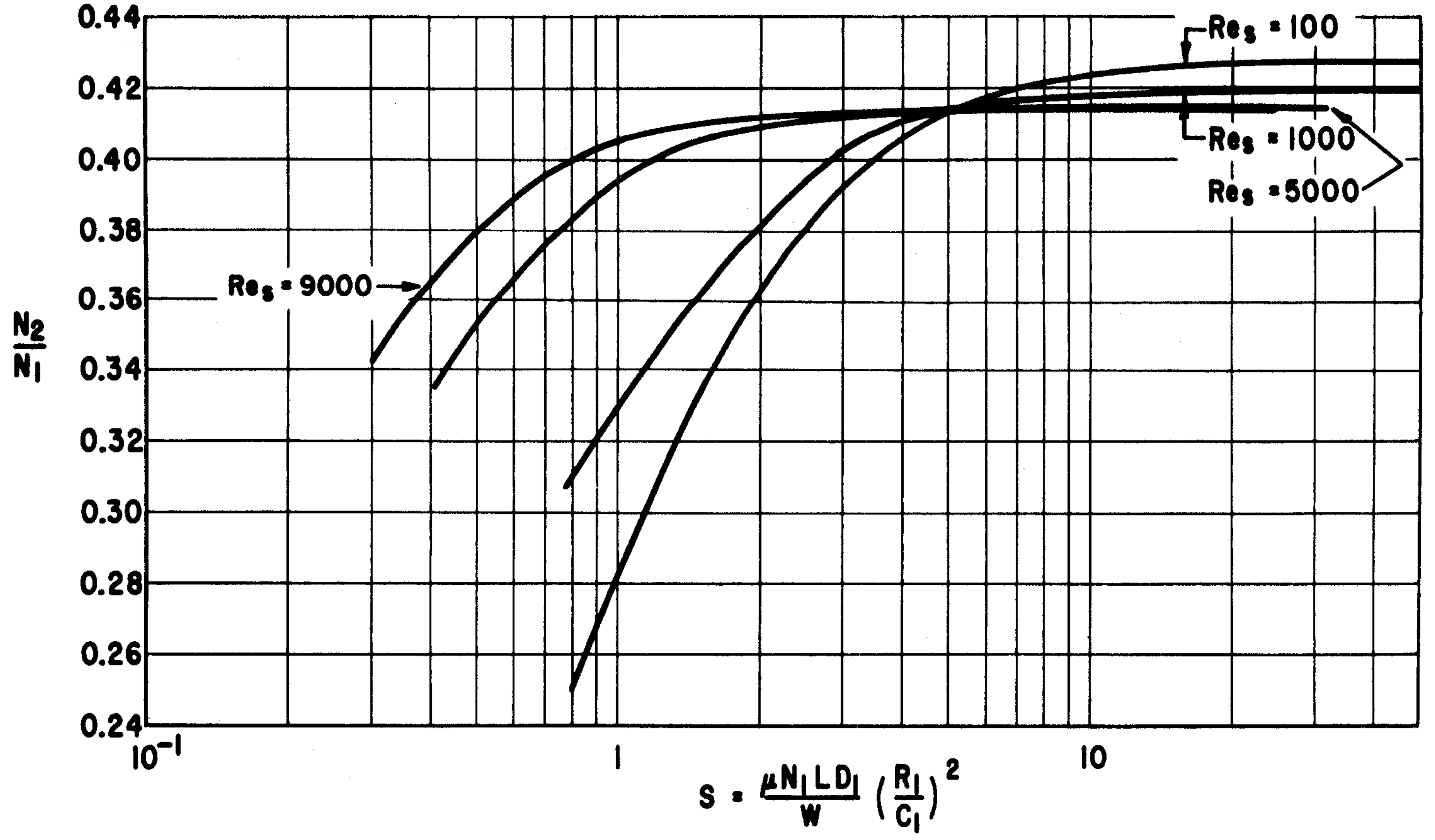

Fig. 39 Floating-Ring Bearing Ring/Shaft Speed Ratio
$C_2/C_1 = 1.3$, $P_s LD_1/W = 1.5$

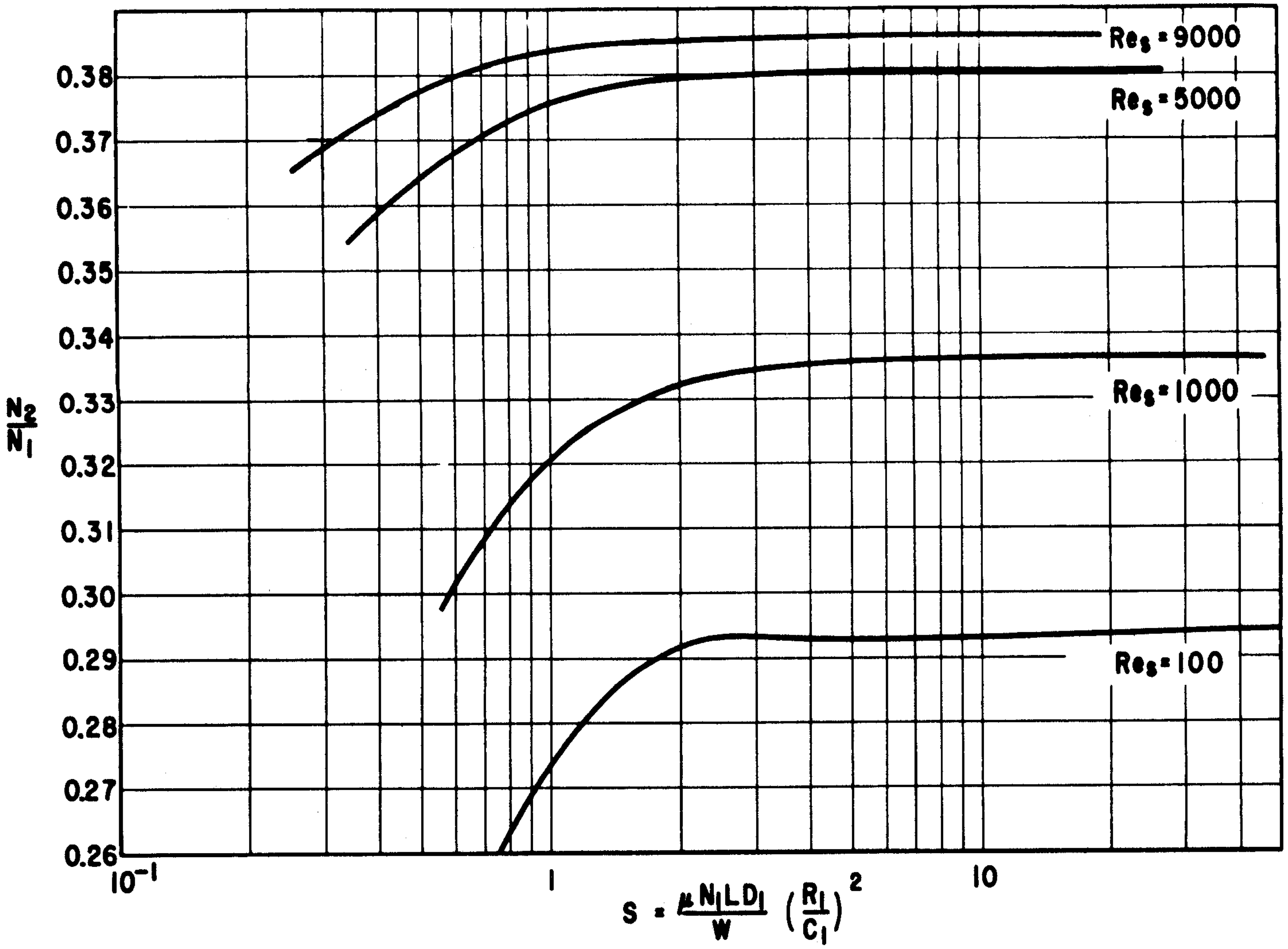

Fig. 40 Floating-Ring Bearing Ring/Shaft Speed Ratio
$C_2/C_1 = 0.7$, $P_s LD_1/W = 10.0$

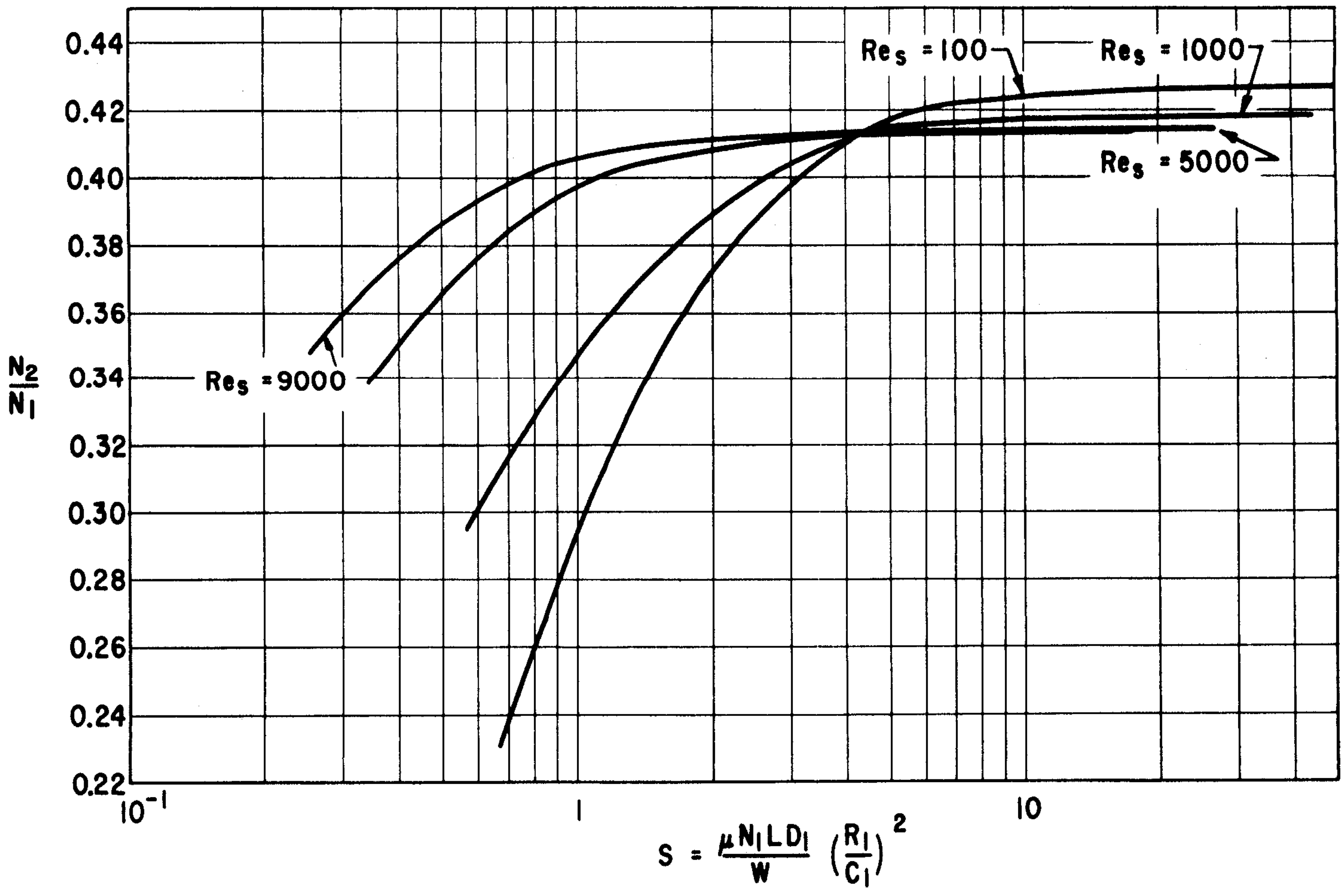

Fig. 41 Floating-Ring Bearing Ring/Shaft Speed Ratio
$C_2/C_1 = 1.3$, $P_s LD_1/W = 10.0$

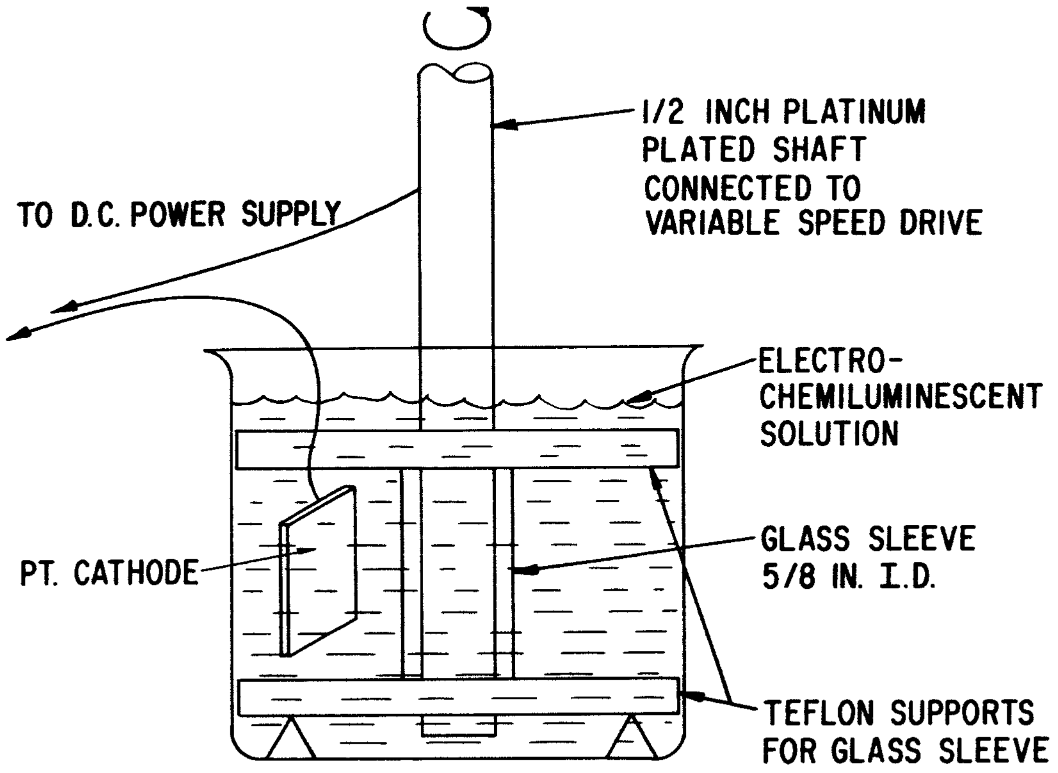
1/2 INCH PLATINUM PLATED SHAFT CONNECTED TO VARIABLE SPEED DRIVE
TO D.C. POWER SUPPLY
ELECTRO-CHEMILUMINESCENT SOLUTION
PT. CATHODE
GLASS SLEEVE 5/8 IN. I.D.
TEFLON SUPPORTS FOR GLASS SLEEVE

Fig. 42 Schematic of Apparatus for Electrochemiluminescence Feasibility Studies

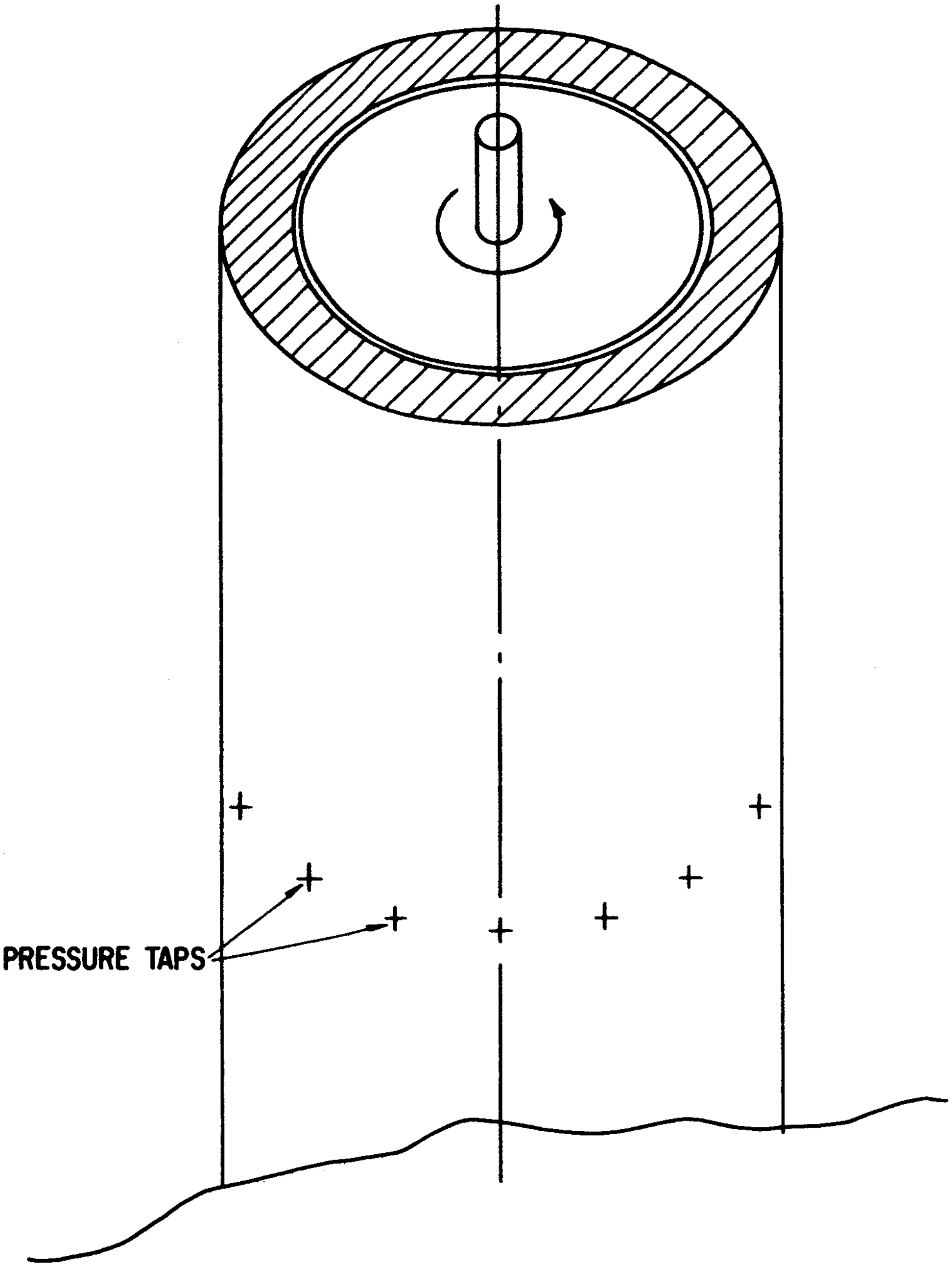
PRESSURE TAPS

Fig. 43 Schematic of Apparatus for Studies of Flow Between Concentric and Eccentric Cylinders

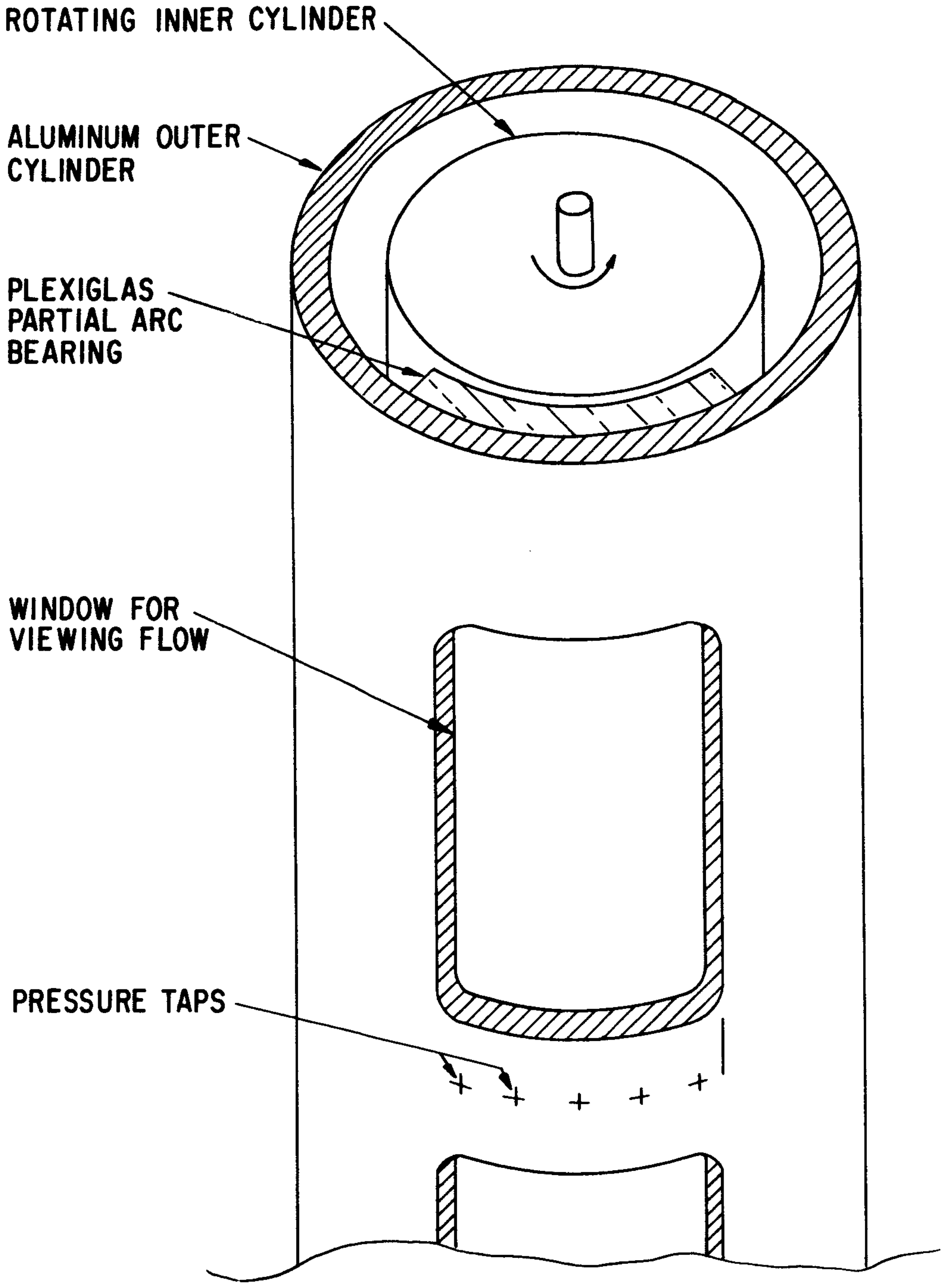
ROTATING INNER CYLINDER
ALUMINUM OUTER CYLINDER
PLEXIGLAS PARTIAL ARC BEARING
WINDOW FOR VIEWING FLOW
PRESSURE TAPS

Fig. 44 Schematic of Partial-Arc Bearing Test Rig